A dataset of vertical profiles of O_3 and HONO from the hyperspectral vertical remote sensing network in China (2021-2024)

Tiliang Zou[1,#], Chengzhi Xing[2,#,*], Xiangguang Ji[3], Shaocong Wei[4], Wei Tan[2], Haoran Liu[3], Cheng Liu[2,3,5,6,7,*]

[1] School of Environmental Science and Optoelectronic Technology, University of Science and Technology of China, Hefei 230026, China

[2] Key Lab of Environmental Optics & Technology, Anhui Institute of Optics and Fine Mechanics, Hefei Institutes of Physical Science, Chinese Academy of Sciences, Hefei, 230031, China

[3] Institute of Physical Science and Information Technology, Anhui University, Hefei 230601, China

[4] Institute of Environment Hefei Comprehensive National Science Center, Hefei, 230031, China

[5] Department of Precision Machinery and Precision Instrumentation, University of Science and Technology of China, Hefei 230026, China

[6] Center for Excellence in Regional Atmospheric Environment, Institute of Urban Environment, Chinese Academy of Sciences, Xiamen 361021, China

[7] Key Laboratory of Precision Scientific Instrumentation of Anhui Higher Education Institutes, University of Science and Technology of China, Hefei 230026, China

[#] These authors contributed equally to this work.

Corresponding to: Chengzhi Xing (xingcz@aiofm.ac.cn); Cheng Liu (chliu81@ustc.edu.cn)

Abstract

Photolysis of HONO and O_3 in the troposphere is one of the primary sources of OH radical and a fundamental control on atmospheric oxidative capacity. Their vertical distributions and diurnal evolution are therefore essential for elucidating photochemical processes in the planetary boundary layer and the lower free troposphere. Yet long-term, continuous observations of the vertical profiles of HONO, O_3, their photolysis frequencies, and the resulting OH production rates remain extremely limited, particularly at multi-regional and interannual scales. Here we present vertical profile measurements of HONO and O_3 acquired by the Chinese Hyperspectral Vertical Remote Sensing Network during 2021–2024. The dataset comprises 22 representative sites spanning urban, suburban, plateau, and basin environments, covering diverse surface and climatic regimes. Profiles extend from the surface to 4 km with ~100 m vertical resolution and ~15 min temporal resolution. Using the TUV model with co-retrieved aerosol and trace-gas profiles, we derive photolysis frequencies of HONO and O_3 and the corresponding OH production rates, $P(OH)_{HONO}$ and $P(OH)_{O3}$. The observations reveal robust regional patterns in the diurnal and vertical structure of tropospheric photochemical activity. Photolysis frequencies peak near local noon and generally increase with altitude from the surface layer to the upper mixed layer and the lower free troposphere, whereas OH production rates reach their maxima within the boundary layer and decrease with height. Processed using a unified retrieval framework and rigorous quality control, this dataset provides quantitative constraints on the contribution of HONO and O_3 photolysis to tropospheric OH, supports improved radical parameterizations in chemical transport models, and enables synergistic multi-platform remote sensing analyses. By delivering the first systematic, long-term vertical profiles of HONO, O_3, and their OH production in China, this public dataset fills a critical observational gap and offers a robust basis for investigating the spatiotemporal evolution of tropospheric oxidative capacity across regions and altitude ranges, with substantial scientific significance and long-term applicability. The dataset is available for free at Zenodo (https://doi.org/10.5281/zenodo.18489836, Zou et al., 2026)

1. Introduction

Over the past decade, “the implementation of China’s Air Pollution Prevention and Control Action Plan” (2013) and “the Three-Year Action Plan for Defending the Blue Sky” (2018) has led to a marked reduction in fine particulate matter ($PM_{2.5}$) nationwide (Liu et al., 2023b; Wang et al., 2020). In contrast, ozone (O_3)—a secondary pollutant and a major atmospheric oxidant—has continued to increase on average in economically developed regions such as the Beijing–Tianjin–Hebei area, the Yangtze River Delta, and the Pearl River Delta, where it has emerged as the most intractable air-quality problem after $PM_{2.5}$ (Guo et al., 2023; He et al., 2023a; Li et al., 2020; Lyu et al., 2025; Zou et al., 2025). To address the observational gaps in these and other key regions, we developed a comprehensive dataset. The dataset comprises

measurements from 22 ground-based sites across five major regions of China—North, East, Southwest, South, and Central China. Photochemical air pollution is a dominant driver of urban and regional air-quality degradation, characterized by the rapid sunlight-driven accumulation of secondary species, most notably O_3 (Dewan and Lakhani, 2022; Donzelli and Suarez-Varela, 2024; Sharma et al., 2025; Wang et al., 2025b). Beyond being a typical secondary pollutant, O_3 is a powerful oxidant that exerts substantial impacts on regional climate, ecosystems, and human health (Monks et al., 2015; Sharma et al., 2025; Wang et al., 2025b; Xing et al., 2017). Nitrous acid (HONO), a short-lived reactive nitrogen species, occurs at relatively low concentrations but represents a major primary source of the OH radical, the key "detergent" of the troposphere (Andersen et al., 2023; He et al., 2023c; Song et al., 2023a; Zhang et al., 2023a). In polluted environments, photolysis of HONO can account for 20–80% of total OH production, and its relative importance is particularly pronounced during early morning and late afternoon, when solar elevation is low and alternative OH sources are less efficient (Elshorbany et al., 2010; He et al., 2023c; Zhang et al., 2023a). A quantitative understanding of the formation and transport of both HONO and O_3 is therefore essential for elucidating the mechanisms of tropospheric photochemical pollution and for designing effective mitigation strategies.

Despite extensive research on HONO and O_3, major gaps persist in observations of their vertical structure and in the parameterization of key photochemical processes, limiting a mechanistic understanding of photochemical air pollution (Liu et al., 2023a; Wang et al., 2018, 2025c; Zhang et al., 2024; Zhu et al., 2025b). Vertical measurements remain particularly sparse, and concurrent profiles of HONO and O_3 are largely unavailable (Garcia-Nieto et al., 2018a; Song et al., 2023a; Wang et al., 2018, 2025c; Zhu et al., 2025b). China National Environmental Monitoring Center (CNEMC), with more than 2,000 surface stations, provides routine measurements of $PM_{2.5}$, NO_2, and SO_2, but lacks observations of key photochemical precursors such as HONO and volatile organic compounds (VOCs) (Liu et al., 2023a; Qu et al., 2020; Zhang et al., 2024; Zhu et al., 2025b). More fundamentally, surface observations alone cannot resolve pollutant distributions within the planetary boundary layer or capture variations in vertical atmospheric structure (Wang et al., 2018, 2019, 2025c; Xuan et al., 2025a; Zhu et al., 2025b), and exclusive reliance on near-surface data may therefore bias assessments of regional transport and accumulation (Liu et al., 2023a; Wang et al., 2019, 2025c). Spaceborne sensors, including MODIS, CALIPSO, TROPOMI, and OMI, provide global fields of aerosol optical depth (AOD) and vertical column densities (VCDs) for selected trace gases. However, their limited temporal sampling and spatial resolution preclude resolving the fine-scale diurnal variability and fine vertical structure of O_3 and HONO (Itahashi et al., 2020; Johnson et al., 2024; Torres et al., 2020a; Wang et al., 2025a). Chemical transport models (CTMs) and regional climate models (RCMs) can reproduce the spatiotemporal evolution of pollutants, but their performance depends critically on initial and boundary conditions, and uncertainties in vertical parameterizations—such as

turbulent mixing and chemical mechanisms—often lead to substantial biases in simulated profiles (Chambers et al., 2019; Kim et al., 2024; Li et al., 2021; Sekiya et al., 2025; Thürkow et al., 2024). Current in situ and remote-sensing techniques also have intrinsic limitations. Lidar systems provide high-resolution aerosol profiles but are restricted in detectable gaseous species and spatial coverage (Anon, 2023; Johnson et al., 2024; Torres et al., 2020b). Aircraft and balloon soundings yield detailed upper-air observations but are expensive and unsuitable for sustained, long-term monitoring (Johnson et al., 2024; Sekiya et al., 2025; Wang et al., 2025a; Yu et al., 2025). Tower measurements, while valuable near the surface, are height-limited and cannot capture the full vertical variability across the boundary layer (Chambers et al., 2019; Kim et al., 2024; Thürkow et al., 2024).

To address the observational limitations and scientific questions outlined above, we developed a comprehensive dataset of vertical profiles of HONO, O_3, and their photolysis frequencies using the Chinese Hyperspectral Vertical Remote Sensing Network. The primary objective is to resolve the vertical structure of HONO and O_3 and to quantify the altitude-resolved production of OH radicals from their photolysis. This dataset fills a critical gap in vertical observations of key photochemical species over China and provides a unique basis for assessing the contribution of HONO photolysis to boundary-layer OH budget, the vertical characteristics of O_3 formation, and the role of aerosols in modulating photolysis rates. The dataset comprises measurements from 22 ground-based sites across five major regions of China—North, East, Southwest, South, and Central China—collected during 2021–2024. Its core products are high-temporal-resolution vertical profiles of HONO and O_3 spanning 0–4 km. Public release of this dataset will enable systematic investigations of the unresolved sources of HONO in the boundary layer and the vertical variability in O_3 production sensitivity. When combined with numerical models, the high-resolution vertical information can be used to evaluate and refine photochemical mechanisms, quantify the contribution of HONO photolysis to the tropospheric OH budget, and reduce uncertainties in vertical parameterizations. These advances will, in turn, support robust source attribution of O_3 pollution and inform the development of coordinated regional control strategies for $PM_{2.5}$ and O_3. The following sections describe the site distribution, observational and retrieval methods, and the seasonal and diurnal features of the HONO and O_3 vertical structures revealed by this dataset.

2. Method

2.1 Description of the monitoring site

The dataset is derived from 22 hyperspectral ground-based vertical remote sensing stations distributed across five major regions of China—North, East, Southwest, South, and Central China—forming an integrated network that samples a wide range of representative atmospheric environments (Table 1). The sites span urban cores, urban–suburban transition zones, regional background areas, coastal and land–sea interaction regions, as well as plateau, mountain, and basin settings, thereby

providing a three-dimensional observational framework for key photochemical species. In North China, stations at the Chinese Academy of Meteorological Sciences (CAMS1, CAMS2) and the University of Chinese Academy of Sciences (UCAS), located within Beijing (~100–120 m a.s.l.), characterize the heavily urbanized and industrialized core of the Beijing–Tianjin–Hebei megacity cluster. The Wangdu (WD) site in suburban Baoding represents regional background conditions, whereas the Shijiazhuang Luancheng (SJZ_LC) site was included to better resolve pollution features specific to industrial cities. The Shanxi University (SXU) site in the Taihang Mountains (780 m a.s.l.) provides critical constraints on pollutant formation and transport between mountainous terrain and adjacent plains. In East China, stations are distributed across the Yangtze River Delta and its hinterland, covering topography from coastal lowlands to inland mountains. The summit of Mount Tai (TS; 1,500 m a.s.l.) offers vertical profiles under relatively clean, high-altitude background conditions. The Nanjing University of Information Science and Technology (NUIST) site represents a densely populated and economically developed urban environment, while sites at Huaibei Normal University (HNU), Anhui University (AHU), and Changfeng (CF) in Anhui Province (30–35 m a.s.l.) capture urban–suburban transition regimes. Southwest China is represented by the Chengdu Academy of Environmental Sciences (CDAES; 505 m a.s.l.) on the Chengdu Plain and the Chongqing (CQ; 332 m a.s.l.) site within the Sichuan Basin. These stations are strategically located to investigate pollutant accumulation and transport under high-humidity conditions and strong topographic confinement, and to probe photochemical processes in complex terrain. In South China, a dense network was established over the Pearl River Delta megacity region. In addition to sites at the Guangzhou Institute of Geochemistry (GIG) and the Southern University of Science and Technology (SUST) in Shenzhen, multiple stations in Guangzhou (Zhuliao, Nansha, Timian, Gongyuan, and Daxuecheng; 15–155 m a.s.l.) form an intra-urban array. This configuration allows detailed examination of the combined influences of land–sea breezes, anthropogenic emissions, and local meteorology on the vertical distributions of HONO and O_3. Central China is represented by the Luoyang (LY) site, located in the middle reaches of the Yellow River within a mixed industrial–agricultural region, providing key constraints on regional transport and accumulation over the central plains. Together, the broad geographic coverage and pronounced contrasts in elevation and surface type make this network well suited to resolve the vertical distributions of aerosols, HONO, and O_3 across urban, suburban, coastal, mountainous, and basin environments. It thus offers a robust observational basis for investigating the dynamics of photochemical air pollution over major regions of China.

Table 1. Geographic information of the stations in the Chinese Hyperspectral Ground-Based Vertical Remote Sensing Network.

Region	Site (code)	Longitude (° E)	Latitude (° N)	Altitude (m)
North China	Chinese Academy of Meteorological Sciences (CAMS1)	116.32	39.94	100
	Chinese Academy of Meteorological	116.32	39.94	100

	Sciences (CAMS2)			
	University of Chinese Academy of Sciences (UCAS)	116.67	40.4	120
	Wangdu (WD)	115.15	38.17	35
	Shijiazhuang_Luancheng (SJZ_LC)	114.61	37.91	70
	Shanxi University (SXU)	112.58	37.63	780
East China	Taishan (TS)	117.1	36.25	1500
	Nanjing University of Information Science and Technology (NUIST)	118.71	32.2	73
	Lin'an (LA)	119.75	30.3	140
	Huaibei Normal University (HNU)	116.8	33.98	35
	Anhui University (AHU)	117.18	31.77	30
	Changfeng (CF)	117.18	32.21	30
Southwest China	Chengdu Academy of Environmental Sciences (CDAES)	104.04	30.65	505
	Chongqing (CQ)	106.5	29.6	332
South China	Guangzhou Institute of Geochemistry (GIG)	113.35	23.15	30
	Southern University of Science and Technology (SUST)	113.99	22.59	40
	Guangzhou_Zhuliao (GZ_ZL)	113.34	23.36	20
	Guangzhou_Nansha (GZ_NS)	113.61	22.77	15
	Guangzhou_Timian (GZ_TM)	113.29	23.55	155
	Guangzhou_Gongyuan (GZ_GY)	113.26	23.13	15
	Guangzhou_Daxuecheng (GZ_DXC)	113.39	23.04	10
Central China	Luoyang (LY)	112.45	34.67	100

2.2 Instrument setup

Between 2021 and 2024, the 22 stations were operated during different periods using a standardized instrument configuration comprising a telescope, a spectrometer, and a control computer. The telescope consisted of a right-angle prism and a plano-convex lens with a full field of view <0.3°, and was mounted on motorized stages that independently controlled elevation and azimuth angles, enabling multi-directional measurements of atmospheric constituents. The spectrometer covered the ultraviolet (296–408 nm) and visible (420–565 nm) wavelength ranges, while the computer handled instrument control and spectral data acquisition. All sites employed an identical elevation scanning sequence of 1°, 2°, 3°, 4°, 5°, 6°, 8°, 10°, 15°, 30°, and 90°(Liu et al., 2022a; Xing et al., 2021a, 2023). The integration time at each elevation angle was 1 min, yielding a full scan cycle of approximately 12 min, which is the total time to complete all elevation measurements and be ready to initiate the next scanning cycle. Routine measurements were conducted during daytime (08:00–18:00 local time). For instrument calibration purposes only, the instruments operated at night to record dark current and electronic offsets. To minimize stratospheric contamination, daytime spectra acquired at solar zenith angles greater than 75° were excluded from further analysis.

2.3 Spectral retrieval

Ultraviolet–visible spectra measured by the ground-based instruments were analysed with the QDOAS software (version 3.2) developed by BIRA-IASB.

Differential optical absorption spectroscopy (DOAS) was applied to retrieve the differential slant column densities (DSCDs) of the oxygen dimer (O_4), O_3, and HONO. For each elevation scan, the zenith spectrum (90° elevation) acquired within the same scanning sequence was used as the reference and subtracted from spectra at lower elevation angles, thereby isolating the narrow-band absorption features of trace gases from broadband structures and enabling robust retrieval of target species. The fitting settings follow Xing et al. (2021, 2024a, b) and are summarized in Table 2. To account for the Ring effect arising from rotational Raman scattering and Fraunhofer line filling-in, a Ring spectrum calculated with DOASIS was included in the fit. Broadband spectral structures were represented and removed using a fifth-order polynomial. This allowing accurate separation of narrow-band molecular absorption. Strict quality control was applied: only retrievals with a root-mean-square (RMS) fitting residual below 1×10^{-3} were retained, ensuring the robustness and stability of the dataset. Representative spectral fits and residuals for O_4, O_3, and HONO are shown in Figure 1.

Table 2. Detailed retrieval settings for O_4, O_3, and HONO.

Parameter	Data source	Fitting interval		
		O_4	O_3	HONO
Wavelength range		338–370 nm	320–340 nm	335–373 nm
NO_2	220 K, I_0* correction (SCD of 10^{17} molec·cm^{-2}); (Vandaele et al., 1998)	√	×	√
NO_2	298 K, I_0 correction (SCD of 10^{17} molec·cm^{-2}); (Vandaele et al., 1998)	√	√	√
O_3	223 K, I_0 correction (SCD of 10^{18} molec·cm^{-2}); (Serdyuchenko et al., 2014)	√	√	√
O_3	243 K, I_0 correction (SCD of 10^{18} molec·cm^{-2}); (Serdyuchenko et al., 2014)	×	×	√
O_3	293 K, I_0 correction (SCD of 10^{18} molec·cm^{-2}); (Serdyuchenko et al., 2014)	√	√	×
O_4	293 K, I_0 correction (SCD of 3×10^{43} molec^2·cm^{-5}); (Thalman and Volkamer, 2013)	√	√	√
HCHO	293 K, I_0 correction (SCD of 5×10^{15} molec·cm^{-2}); (Orphal and Chance, 2003)	√	√	√
BrO	273 K, I_0 correction (SCD of 10^{13} molec·cm^{-2}); (Fleischmann et al., 2004)	√	×	√
Ring	Ring spectra calculated with DOASIS	√	√	√
HONO	I_0 correction (SCD of 10^{15} molec·cm^{-2});(Stutz et al., 2000)	×	×	√
Polynomial degree		5	5	5
Intensity offset		Constant	Constant	No

* Solar I_0 correction, Aliwell et al.(2002).

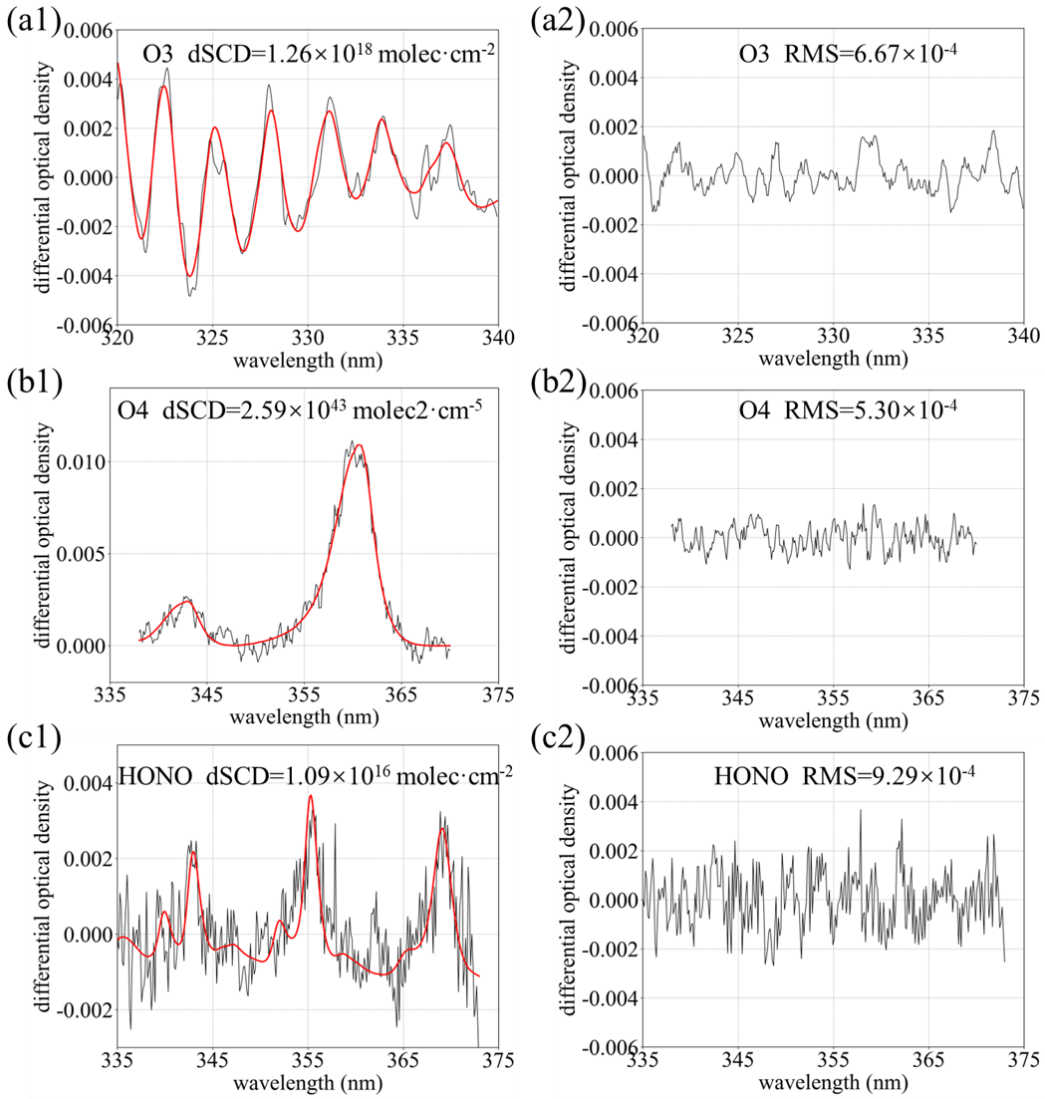

Figure 1. (a1) O_3, (b1) O_4, and (c1) HONO DOAS fitting examples; (a2) O_3, (b2) O_4, and (c2) HONO fitting residuals.

2.4 Vertical profile retrieval algorithm

Vertical profiles of aerosols and trace gases (HONO and O_3) were retrieved using an inversion framework based on the optimal estimation method (OEM). The forward radiative transfer calculations were performed with the linearized pseudo-spherical vector discrete ordinate model VLIDORT (Spurr, 2006). The posterior state vector $\boldsymbol{x}$ was obtained by minimizing the cost function χ^2:

$$\chi^2 = (\boldsymbol{y} - \boldsymbol{F}(\boldsymbol{x},\boldsymbol{b}))^T \boldsymbol{S}_\varepsilon^{-1} (\boldsymbol{y} - \boldsymbol{F}(\boldsymbol{x},\boldsymbol{b})) + (\boldsymbol{x} - \boldsymbol{x_a})^T \boldsymbol{S}_a^{-1} (\boldsymbol{x} - \boldsymbol{x_a}) \quad (1)$$

where y denotes the measured DSCDs, $\boldsymbol{F}(x,b)$ is the forward model, b represents ancillary meteorological parameters (e.g., temperature, pressure, single-scattering albedo, and asymmetry factor), $\boldsymbol{x_a}$ is the a priori state vector, S_ε is the measurement error covariance matrix, and $\boldsymbol{S_a}$ is the a priori covariance matrix. For both aerosols and trace gases, the a priori vertical profiles were assumed to decrease exponentially

with altitude, reflecting the characteristic rapid decay of pollutant concentrations within the planetary boundary layer. Because the absorption of the O_4 is strongly linked to aerosol optical properties, aerosol vertical profiles were first retrieved from multi-elevation O_4 DSCDs and subsequently used as inputs to the forward model for the retrieval of O_3 and HONO profiles. The atmosphere from the surface to 4 km was discretized into 20 layers with a vertical resolution of 200 m (Xing et al., 2024b). Retrievals were subjected to strict quality control: profiles with degrees of freedom (DOF) below 1.0, χ^2 values exceeding 200, or relative uncertainties greater than 50% were excluded from further analysis.

2.5 TUV model

Photolysis rates of HONO and O_3 were computed with the Tropospheric Ultraviolet and Visible (TUV) radiative transfer model developed by NCAR, which is based on rigorous radiative transfer theory and implemented in FORTRAN (https://www2.acom.ucar.edu/modeling/tropospheric, last access: 26 January 2026). The TUV model simulates the propagation of solar radiation in the troposphere under prescribed optical and chemical conditions and provides spectrally resolved photolysis frequencies for key atmospheric reactions. These rates were used to quantify the contributions of HONO and O_3 photolysis to OH production. Model inputs included AOD at ~361 nm derived from MAX-DOAS–retrieved aerosol extinction profiles, total ozone column from daily TROPOMI observations (typically 260–280 DU), and single-scattering albedo (SSA) constrained by regression analyses of O_4 absorptions at 361 and 477 nm (Xing et al., 2019).

3. Vertical profile observations of atmospheric composition

Figure 2 summarizes the monthly completeness of O_3 and HONO vertical profile measurements at 22 sites from 2021 to 2024. Shading denotes the fraction of valid observations, with 100% indicating uninterrupted daytime measurements and successful profile retrievals throughout the month. Because stations were commissioned at different times and operated under varying maintenance and field conditions, the available observation periods differ among sites. Most stations provide long, continuous time series of both HONO and O_3. More than 85% of the sites had operational histories spanning over one year, and 60% for more than two years, although these periods may include intermittent data gaps due to maintenance, weather, or technical issues, with only quality-controlled valid profiles retained in the dataset, demonstrating the temporal stability of the network. This coverage enables robust characterization of seasonal and diurnal variability under diverse climatic regimes and emission backgrounds. Although a few sites had shorter operational periods owing to instrument commissioning and field constraints, they still delivered several months of continuous high-quality data, which are valuable for regional intercomparison and support analyses of long-term trends and photochemical processes. Isolated months with missing or incomplete data occur at some sites,

primarily because of unavoidable factors such as instrument maintenance, power interruptions, persistent cloud or precipitation, and quality-control filtering (e.g., excessive fitting residuals or low DOF in the retrievals).

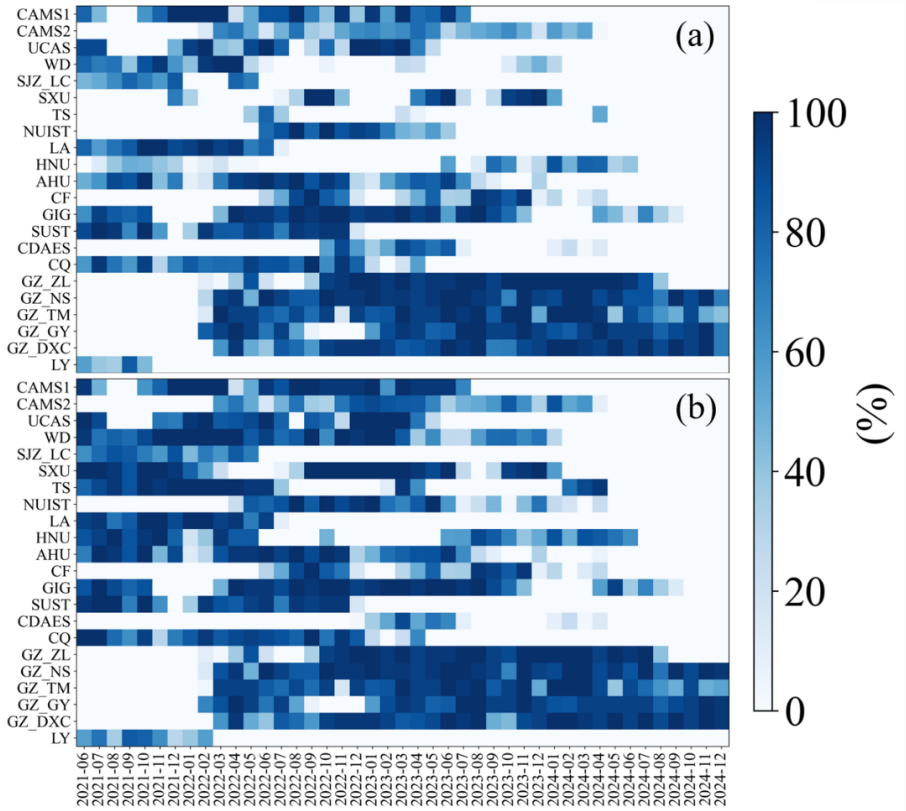

Figure 2. Monthly data completeness of the vertical profiles of (a) O_3 and (b) HONO.

3.1 HONO

Figure 3 presents the 2021–2024 mean vertical profiles of HONO across all sites. At every location, HONO is strongly enriched near the surface and decreases rapidly with height, following an approximately exponential decay. This structure is characteristic of a boundary-layer-dominated species controlled by ground-based sources (Li et al., 2025b; Meng et al., 2020; Xing et al., 2024c; Xu et al., 2021). Peak mixing ratios occur within the lowest 0–0.5 km, decline sharply between 0.5 and 1.5 km, and generally fall to regional background or near the detection limit above 2 km (<0.05–0.1 ppb), becoming negligible by 4 km. Such steep gradients reflect dominant near-surface emissions and nocturnal heterogeneous formation of HONO from NO_2 on ground and aerosol surfaces, combined with its short photochemical lifetime and rapid daytime photolysis, which preclude sustained accumulation in the free troposphere (Li et al., 2025b; Meng et al., 2020; Xing et al., 2024a). Pronounced regional contrasts are evident. Urban sites in North and East China (e.g., CAMS1, CAMS2, WD, SXU, AHU) exhibit the highest near-surface HONO (0.3–0.5 ppb below 0.3 km), followed by a rapid decrease to <0.1 ppb above 1 km. The sharp vertical gradients and absence of secondary maxima aloft indicate strong control by surface sources and nocturnal heterogeneous production, with efficient removal by

turbulent mixing and photolysis within the planetary boundary layer (Xu et al., 2021). In contrast, background or relatively clean sites (e.g., TS, LA) show much lower concentrations, with near-surface values typically <0.2 ppb and a monotonic decrease with altitude, consistent with weak local emissions and dominance of regional background (Garcia-Nieto et al., 2018b; Li et al., 2025b). Sites in South and Southwest China (e.g., GZ_ZL, GZ_NS, GZ_DXC, CQ, CDAES) display a similar monotonic decay: elevated HONO confined to the lowest 0–0.5 km and rapid attenuation to background levels above 1–2 km, without a distinct mid-level enhancement. Although near-surface mixing ratios at some locations (e.g., GZ_DXC, CQ) approach or slightly exceed 0.3 ppb, their vertical decay rates are comparable to those at northern and eastern urban sites. This indicates that, even under high humidity or complex topography, HONO remains largely restricted to the lower boundary layer, governed by its short lifetime, fast photolysis, and dilution by convective mixing, while large-scale vertical transport contributes little to its maintenance aloft (Li et al., 2025b; Xing et al., 2021b; Xu et al., 2021). Seasonal mean profiles are shown in Figures S1–S4. Taken together, the regionally averaged profiles consistently demonstrate strong near-surface accumulation and rapid vertical attenuation of HONO. This confirms that HONO is a short-lived, boundary-layer-derived reactive nitrogen species, tightly coupled to surface emissions and heterogeneous chemistry. It therefore plays a key role in initiating early-morning OH production and regulating boundary-layer oxidizing capacity, whereas its direct impact in the free troposphere is comparatively minor.

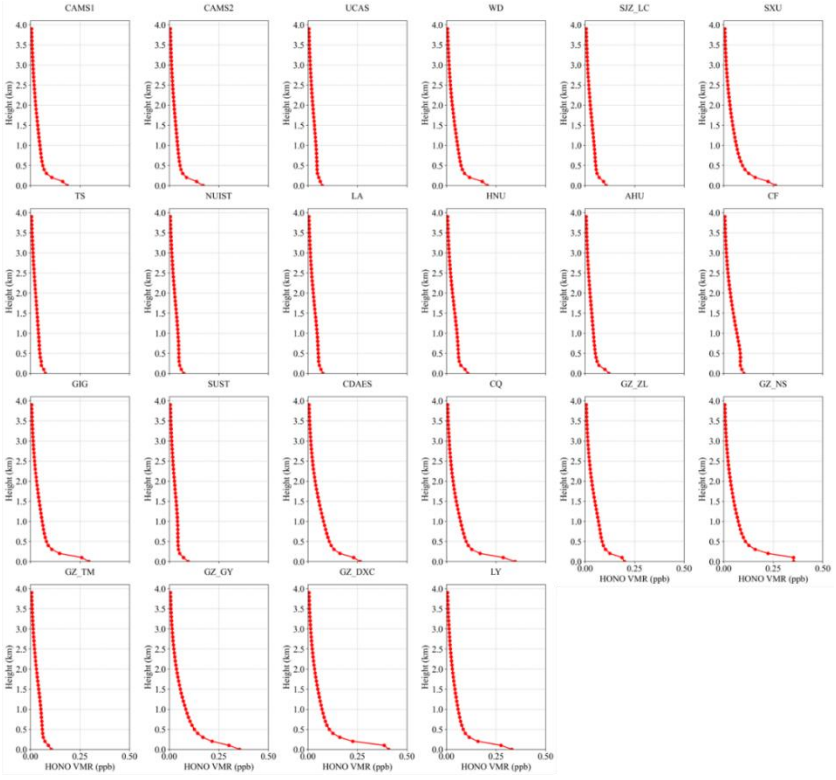

Figure 3. Mean vertical profiles of HONO averaged over 2021–2024.

Figure 4 illustrates the mean diurnal evolution of HONO. As a key reactive

nitrogen species, HONO exhibits vertical and temporal patterns that integrate the effects of surface emissions, heterogeneous and photochemical processes, and boundary-layer dynamics. Based on HONO data obtained from the hyperspectral vertical remote-sensing network, pronounced regional and site-specific patterns are observed. Across North China (CAMS1, CAMS2, UCAS, WD, SJZ_LC and SXU), HONO exhibits a clear near-surface morning maximum followed by an afternoon minimum. At CAMS1 and CAMS2, the 0–1 km volume mixing ratio (VMR) peaks at 08:00–10:00 local time (0.3–0.4 ppb) and decreases to 0.1–0.2 ppb by 14:00–16:00. This pattern reflects nocturnal accumulation driven by heterogeneous conversion of NO_2 on aerosol and ground surfaces (Liu et al., 2022a; Xing et al., 2023; Xuan et al., 2025b); after sunrise, enhanced solar radiation leads to the release and photochemical processing of HONO; meanwhile, morning rush-hour emissions of NO_2 and VOCs further promote HONO formation(Garcia-Nieto et al., 2018a; Zhang et al., 2025a). At the mountain site SXU, topography-induced temperature inversions enhance nighttime accumulation, yielding a more pronounced morning peak. In contrast, UCAS and WD, characterized by weaker anthropogenic emissions, show lower near-surface HONO levels and smaller diurnal amplitudes. In East China (TS, NUIST, LA, HNU, AHU and CF), urban sites display modest morning enhancements (0.2–0.3 ppb at 08:00–10:00) followed by afternoon decreases driven by boundary-layer growth and photolysis. At the high-altitude TS site (1500 m), HONO remains below 0.1 ppb with weak diurnal variability, reflecting clean background conditions and efficient vertical mixing. Sites with dense vegetation or agricultural land use (LA and CF) may receive contributions from biogenic VOC-related chemistry, but the overall pattern still features a subdued morning maximum(Liang et al., 2017; Ryan et al., 2018a; Xue et al., 2021; Ye et al., 2023a). At South China and Southwest China sites (GIG, SUST, CDAES, CQ and the Guangzhou cluster: GZ_ZL, GZ_NS, GZ_TM, GZ_GY and GZ_DXC), warm and humid conditions together with basin or coastal circulations further modulate the diurnal cycle. Urban stations typically reach 0.3–0.5 ppb near the surface in the morning and decline to 0.1–0.2 ppb in the afternoon. In the Sichuan Basin (CQ), strong nocturnal inversions favour HONO accumulation, producing slightly higher morning peaks (0.4–0.5 ppb). At coastal sites, land–sea breeze circulation leads to a transient morning enhancement followed by dilution by cleaner marine air masses. At the Central China site LY, the diurnal pattern resembles that in North and South China, with a clear morning maximum and lower concentrations in the afternoon associated with boundary-layer development. Seasonal mean diurnal vertical profiles are shown in Figures S5–S8. Overall, the diurnal cycle of HONO is governed by three coupled processes: (i) nocturnal heterogeneous production from NO_2 on aerosol and surface substrates, which drives early-morning maxima (Li et al., 2025b; Meng et al., 2020; Xuan et al., 2024); (ii) enhancement by morning anthropogenic emissions of NOx and VOCs from traffic and industrial activities (Hao et al., 2020; Zhang et al., 2025a, 2023b); and (iii) rapid photolysis and boundary-layer dilution in the afternoon (Xing et al., 2021b, 2024a; Zhang et al., 2023b). Regional

contrasts arise from the combined effects of emission intensity, topography (basin, mountain and coastal settings), and meteorological conditions, particularly temperature inversions and ventilation efficiency (Li et al., 2025b; Xuan et al., 2024; Zhang et al., 2025a).

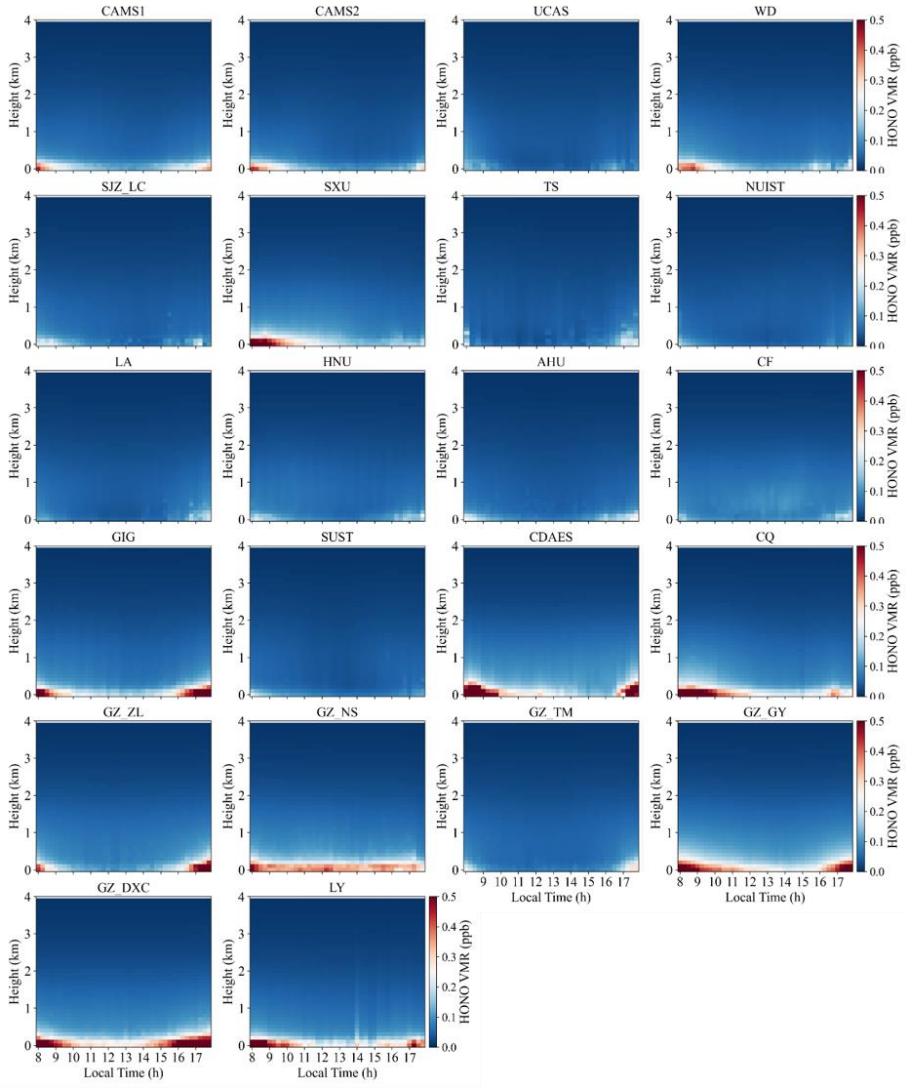

Figure 4. Mean diurnal vertical profiles of HONO for 2021–2024.

3.2 O_3

Figure 5 presents the mean vertical profiles of O_3 averaged over 2021–2024 for all sites. A consistent "low near the surface–high aloft" structure is observed, characterized by a monotonic increase or a weak S-shaped pattern. O_3 VMR are lowest in the lowest 0–0.5 km (20–60 ppb), rise rapidly between 1 and 2 km, and reach daytime maxima at 3–4 km (60–100 ppb). This vertical gradient agrees well with MAX-DOAS and ozone-sonde observations over eastern China and other regions worldwide (Couillard et al., 2021; Ji et al., 2023; Liao et al., 2024; Su et al., 2017; Wang et al., 2018; Zeng et al., 2023), and reflects the combined effects of strong near-surface NO_2 titration, dry deposition, and boundary-layer mixing that

suppress O_3, together with photochemical production and regional transport that enhance O_3 aloft (Couillard et al., 2021; Donzelli and Suarez-Varela, 2024; Liao et al., 2024; Zeng et al., 2023; Zhu et al., 2025b). Within the boundary layer (0–1 km), O_3 generally increases sharply with height, and a weak local maximum or inflection is often found at 0.2–0.5 km. This contrasts with the vertical distributions of NO_2 and HCHO at the same sites, which show high near-surface concentrations dominated by emissions (Couillard et al., 2021; Hu et al., 2024; Hong et al., 2022; Jiao et al., 2025; Liu et al., 2023b). In contrast, O_3 is efficiently removed near the ground by nocturnal NO_2 titration and daytime surface deposition (Liao et al., 2024; Xing et al., 2022). At urban and suburban stations (e.g., UCAS and CF), O_3 in the lowest 0–0.3 km can decrease to 20–40 ppb, indicating strong titration by traffic and industry related NO_2 (Hu et al., 2024). Between 1 and 3 km, O_3 increases nearly monotonically at most sites, with the largest vertical gradient typically occurring around 2–3 km. This layer often corresponds to the daytime boundary-layer top or the nocturnal residual layer and represents a key altitude for regional photochemical accumulation and downward transport (He et al., 2023b; Liao et al., 2024; Zhu et al., 2025a). Numerous studies have shown that O_3-rich air in the upper boundary layer and residual layer can be mixed downward during boundary-layer growth, and that O_3 stored aloft at night is re-entrained to the surface the following morning, making an important contribution to surface O_3 levels (Ancellet et al., 2024; Donzelli and Suarez-Varela, 2024; Liu et al., 2022b; Shi et al., 2022; Song et al., 2024; Wang et al., 2024b). At 3–4 km, O_3 VMR further increase and tend to level off, with some sites exhibiting distinct maxima. At these altitudes, the influence of surface NO_2 titration becomes negligible, whereas long-range transport and possible stratosphere–troposphere exchange start to play a role. Previous studies have shown that enhanced O_3 at 3–5 km over East Asia in spring and summer can partly arise from stratospheric intrusions and westerly long-range transport (Li et al., 2025a; Liao et al., 2024, 2025; Park et al., 2020). The pronounced O_3 enhancements observed at 3–4 km at sites such as CQ, GZ_TM and SUST are therefore likely linked to free-tropospheric background O_3 and regional-scale transport processes. Seasonal mean O_3 vertical profiles are shown in Figures S9–S12.

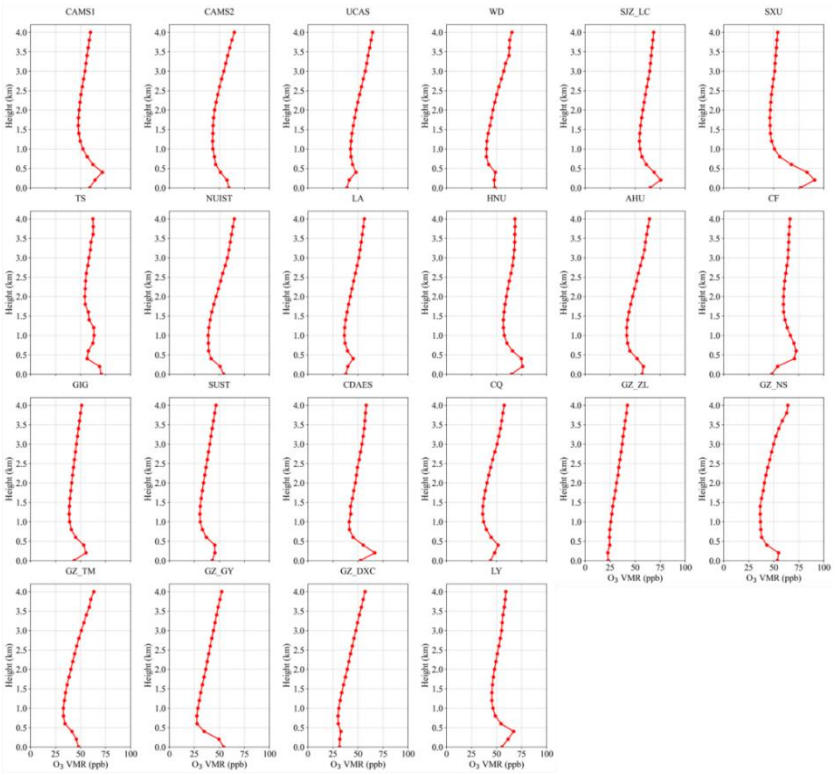

Figure 5. Mean vertical profiles of O_3 averaged over 2021–2024.

Figure 6 presents the mean diurnal evolution of O_3. All sites exhibit pronounced daily cycles with clear regional contrasts. O_3 typically peaks in the morning (08:00–10:00) or in the early afternoon (12:00–15:00), in phase with the diurnal variation of solar irradiance and photochemical reaction rates (Xia et al., 2021; Yang et al., 2020). This behaviour is most evident in North and East China, whereas the cycle is weaker in South China, likely owing to persistently high temperature and humidity that modulate boundary-layer development and photochemistry (Zhou et al., 2022). At several sites (e.g., TS, CDAES and CQ), enhanced O_3 at 1–2 km during 12:00–15:00 points to the influence of local meteorology and emission distributions (Chen et al., 2023; Li et al., 2025a). In contrast, morning maxima at CAMS1, CAMS2, UCAS, NUIST and AHU reflect the rapid re-entrainment and photochemical processing of O_3 accumulated overnight after sunrise (David and Nair, 2011; Liao et al., 2023). The vertical structure of the diurnal cycle also differs markedly among regions. North China sites show strong near-surface variability, whereas peak O_3 in South China is generally lower, consistent with regional differences in pollution levels and meteorological conditions. Relatively high near-surface O_3 at GZ_ZL and GZ_NS is likely linked to local emissions combined with weak dispersion (Yang et al., 2020; Zhou et al., 2022). North China stations (CAMS1, CAMS2, UCAS, WD, SJZ_LC and SXU) display a typical urban O_3 diurnal pattern. At CAMS1 and CAMS2, O_3 in the 0–1 km layer reaches 80–120 ppb in the morning (08:00–10:00) and decreases markedly in the early afternoon, reflecting rapid boundary-layer growth and photochemical loss after sunrise (David and Nair, 2011; Liao et al., 2023). UCAS and WD show similar morning maxima, whereas SJZ_LC is characterized by lower and

more stable O_3, indicative of relatively clean background conditions. At SXU, high morning O_3 (80–100 ppb) is followed by even higher afternoon levels (>100 ppb), pointing to strong in situ secondary production under intense photochemical activity (Wang et al., 2017; Xia et al., 2021). East China sites (TS, NUIST, LA, HNU, AHU and CF) exhibit more complex diurnal behaviour. At TS, O_3 peaks at 1–2 km during 12:00–15:00 (80–100 ppb), suggesting an important role of vertical transport and local emissions. NUIST and AHU show morning maxima similar to those in North China, whereas LA maintains low and weakly varying O_3, consistent with relatively clean conditions (Chen et al., 2024). At HNU, near-surface O_3 increases in the early afternoon (60–80 ppb), reflecting active photochemistry (Wang et al., 2025c). CF shows a pronounced afternoon peak (13:00–17:00, 80–120 ppb), indicating a strong influence of local sources (Xia et al., 2021; Yang et al., 2020). South China sites (GIG, SUST, GZ_ZL, GZ_NS, GZ_TM, GZ_GY and GZ_DXC) differ substantially from those in the north and east. GIG exhibits low and weakly varying O_3, representative of background conditions (Chen et al., 2024; Lin et al., 2022). The other sites show morning near-surface maxima (80–100 ppb at 08:00–10:00), followed by decreases associated with rapid boundary-layer development after sunrise (David and Nair, 2011; Liao et al., 2023), and enhanced O_3 at 3–4 km in the afternoon (13:00–17:00), highlighting the pronounced vertical structure of O_3 pollution in this region. Southwestern sites (CDAES and CQ) display distinct afternoon enhancements at 1–2 km. At CDAES, O_3 reaches 80–120 ppb during 15:00–18:00, likely favored by high temperature and humidity that accelerate photochemical production (Yang et al., 2020; Zhang et al., 2022), while CQ shows a similar but weaker enhancement (60–80 ppb). The central China site LY exhibits morning near-surface maxima (60–80 ppb) and elevated O_3 at 2–4 km in the afternoon, characteristic of a typical urban diurnal cycle. Seasonal mean diurnal vertical profiles are shown in Figures S13–S16. These regional contrasts underline the differing controls on O_3 across China, with strong local photochemistry in North China, combined regional transport and sustained photochemical production in South China, and mixed influences of emissions and meteorology in East China.

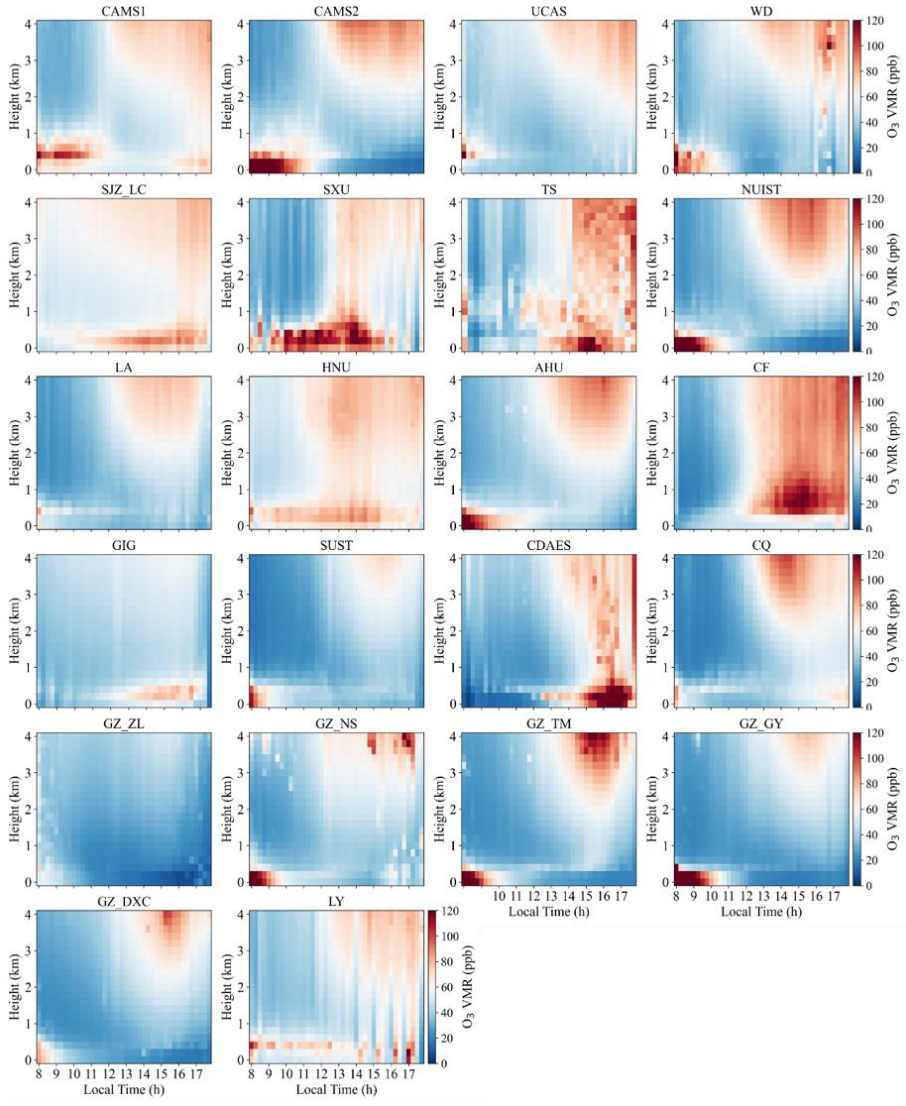

Figure 6. Mean diurnal vertical profiles of O_3 for 2021–2024.

3.3 OH production

Photolysis of HONO and O_3 constitutes a primary source of OH radicals and therefore controls the atmospheric oxidation capacity (AOC). To quantify the AOC at each site, we evaluated altitude-resolved OH production from HONO and O_3 using retrieved profiles combined with photolysis frequencies calculated by the TUV model. OH production from HONO and O_3 was computed from the following expressions.

$$P(OH)_{HONO} = J(HONO) \times [HONO] \quad (2)$$

$$P(OH)_{O_3} = 2 \times f \times J(O(^1D)) \times [O_3] \quad (3)$$

Here, J(HONO) and J($O(^1D)$) are the photolysis rate coefficients of HONO and O_3, respectively, obtained from the TUV model. $O(^1D)$ denotes electronically excited atomic oxygen produced by O_3 photodissociation, and f represents the branching fraction of the reaction $O(^1D) + H_2O \rightarrow 2OH$. [HONO] and [$O_3$] are the

concentrations of HONO and O_3 at each altitude level.

Figure 7 presents the mean diurnal vertical profiles of the HONO photolysis frequency, J(HONO), at 22 sites during 2021–2024; the corresponding seasonal mean diurnal variations are presented in Figures S17–S20. All sites exhibit a canonical photochemical pattern: J(HONO) increases rapidly after sunrise, reaches a maximum around local noon, and then gradually decreases with increasing solar zenith angle. Elevated values persist between 10:00 and 14:00 local time, with peak J(HONO) typically occurring near 12:00–13:00, indicating that HONO photolysis is primarily controlled by solar irradiance, in agreement with observations in Beijing and Guangzhou (He et al., 2023c; Ryan et al., 2018b). Vertically, J(HONO) increases systematically with altitude. Photolysis rates are relatively low in the near-surface layer (0–0.5 km), increase markedly in the upper mixed layer and lower free troposphere (approximately 1–3 km), and reach maxima between 2 and 4 km, with peak values around 2.5×10^{-3} s^{-1}. This "weaker near the surface and stronger aloft" structure is highly consistent with the J(HONO) profiles reported by Xing et al. (2024a) and reflects the combined effects of aerosol attenuation of ultraviolet radiation in the lower atmosphere and enhanced shortwave actinic flux at higher altitudes (He et al., 2023c; Ryan et al., 2018b; Spataro and Ianniello, 2014). At the North China sites (CAMS1, CAMS2, UCAS, WD, SJZ_LC, SXU), J(HONO) exhibits a pronounced diurnal cycle, increasing after sunrise with rising solar radiation, peaking at midday (12:00–14:00) at 0.0020–0.0025 s^{-1}, and decreasing in the afternoon (14:00–18:00). The urban Beijing sites CAMS1 and CAMS2 show peak values of ~0.0025 s^{-1}, comparable to those at other North China Plain stations (e.g., UCAS and WD), reflecting strong photolysis under high HONO loading and favourable radiation conditions. At SJZ_LC, located at the foothills of the Taihang Mountains, morning J(HONO) is slightly enhanced, likely owing to temperature inversions that modulate the vertical distribution of aerosols and actinic flux. The elevated site SXU (780 m a.s.l.) exhibits systematically higher J(HONO) than lowland stations, with a peak of ~0.0022 s^{-1}, consistent with reduced aerosol extinction and stronger solar radiation at higher altitude. East China sites (TS, NUIST, LA, HNU, AHU, CF) display similar peak timing to North China but slightly lower magnitudes (0.0015–0.0025 s^{-1}). For example, J(HONO) at NUIST peaks at ~0.0020 s^{-1}, whereas the high-altitude background site TS (1500 m a.s.l.) reaches ~0.0021 s^{-1}, consistent with enhanced actinic flux under cleaner atmospheric conditions. In South China (GIG, SUST, GZ_ZL, GZ_NS, GZ_TM, GZ_GY, GZ_DXC), the maximum J(HONO) occurs slightly later in the day (13:00–15:00) and attains higher values (0.0020–0.0030 s^{-1}). The highest peak is observed at GZ_DXC (~0.0030 s^{-1}), likely reflecting elevated HONO concentrations promoted by warm and humid conditions that favor heterogeneous formation. The southwestern basin site CQ shows a comparable peak (~0.0025 s^{-1}), while the Central China site LY reaches ~0.0020 s^{-1}, similar to values in North and East China. Overall, urban sites exhibit larger diurnal amplitudes and 20–40% higher J(HONO) maxima than mountain or clean-background sites, owing to

higher HONO abundances and aerosol loading that modulate the effective actinic flux. This behaviour is fully consistent with previous findings from Beijing, Shanghai and other megacities, which reported pronounced daytime enhancement of J(HONO) under high-NO_2 and high-HONO conditions (He et al., 2023c; Spataro and Ianniello, 2014; Ye et al., 2023b).

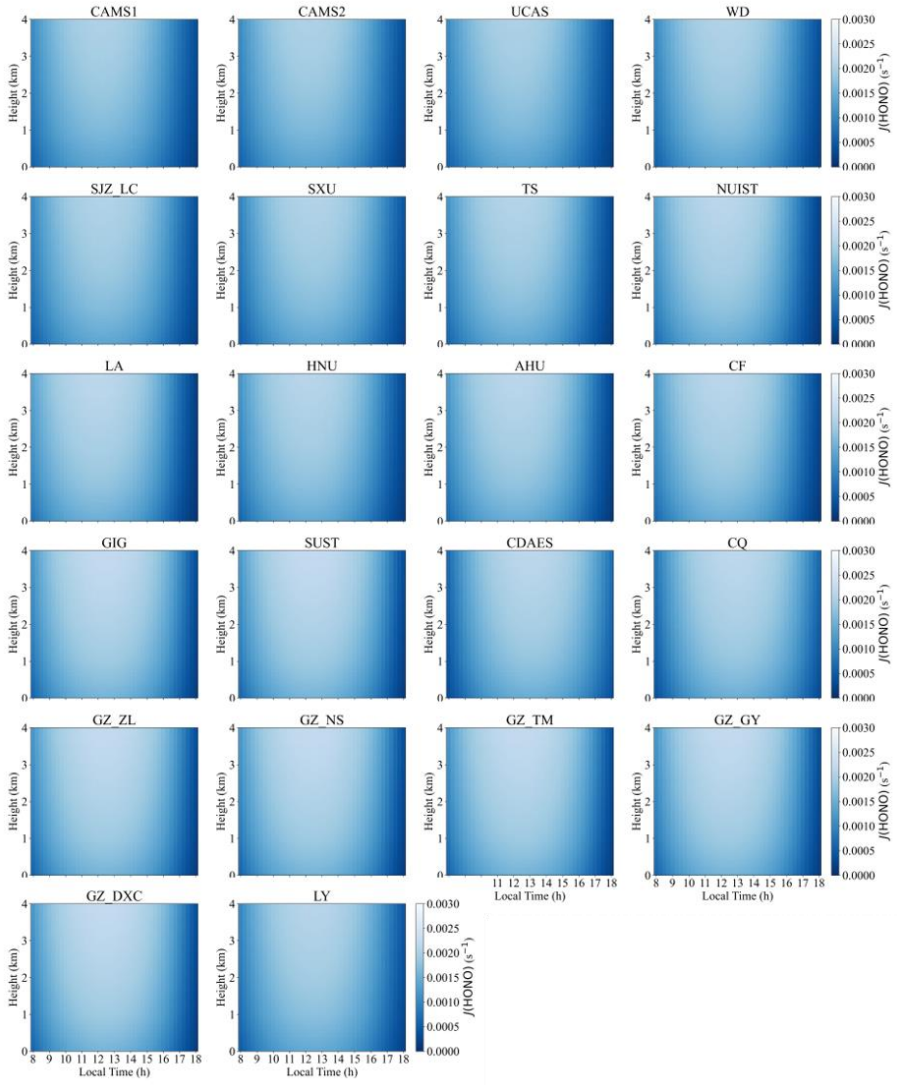

Figure 7. Mean diurnal vertical profiles of the HONO photolysis rate, J(HONO).

Figure 8 presents the mean diurnal vertical profiles of OH production from HONO photolysis, $P(OH)_{HONO}$, at 22 sites; the corresponding seasonal mean profiles are shown in Figures S21–S24. At all sites, $P(OH)_{HONO}$ displays a pronounced unimodal diurnal cycle, increasing rapidly after sunrise, peaking between 10:00 and 14:00, and declining thereafter. The peak timing closely follows the maximum of the J(HONO), whereas the peak altitude remains confined to the near-surface layer, reflecting the strong surface enhancement of HONO. In the lower boundary layer (0–0.5 km), $P(OH)_{HONO}$ attains its column maximum, with most sites peaking between 11:00 and 13:00 and reaching 1.0×10^{-4}–5.5×10^{-4} ppb·s^{-1}. For all stations, $P(OH)_{HONO}$ is largest within 0–1 km and decreases monotonically with height, consistent with the

preferential accumulation of HONO near the surface and the resulting localization of photochemically produced OH (He et al., 2023c; Li et al., 2025b; Xing et al., 2021b; Zhang et al., 2025a). Several sites, including SXU, CDAES, CQ, GZ_NS, GZ_GY, and GZ_DXC, exhibit particularly strong OH production, with peak $P(OH)_{HONO}$ commonly exceeding 3.0×10^{-4} ppb·s^{-1}. This reflects the combined effects of elevated HONO levels and intense solar radiation. At these locations, the high- $P(OH)_{HONO}$ layer can extend to 1–2 km, indicating a deeper photochemically active region. This feature is consistent with earlier reports highlighting the substantial contribution of HONO to OH in the lower free troposphere (Aumont et al., 2003; R. Crilley et al., 2016; Xue et al., 2025; Zhang et al., 2025a). Vertically, $P(OH)_{HONO}$ decreases rapidly with altitude at all sites and is reduced to 20–40% of its surface value above 2 km, demonstrating that the impact of HONO photolysis on OH is largely confined to the boundary layer. In agreement with previous observations in Beijing and Guangzhou (Gu et al., 2022; Meng et al., 2020; Yu et al., 2022), HONO photolysis represents one of the dominant OH sources during the morning and around local noon, accounting for 30–60% of the daytime OH production near the surface (Song et al., 2023a; Tang et al., 2015). In the present study, several plateau sites show even larger relative contributions at midday, indicating that under conditions of low NO_2 and strong solar irradiance, HONO photolysis becomes an especially efficient radical source, consistent with findings at Nam Co (Xing et al., 2024b). Regionally, North China sites (CAMS1, CAMS2, UCAS, WD, SJZ_LC, and SXU) exhibit near-surface (0–1 km) $P(OH)_{HONO}$ maxima between 12:00 and 14:00 local time, with values of 1.0×10^{-4}–3.0×10^{-4} ppb·s^{-1}. At CAMS1, the peak reaches ~1.5×10^{-4} ppb·s^{-1}, whereas at SJZ_LC, although nocturnal temperature inversions near the Taihang Mountains may favour HONO accumulation, the peak remains modest (~1.2×10^{-4} ppb·s^{-1}) owing to weaker local emissions, comparable to UCAS and WD (1.0×10^{-4}–2.5×10^{-4} ppb·s^{-1}). At these sites, $P(OH)_{HONO}$ declines sharply with height and is substantially reduced above 1 km, underscoring the near-surface confinement of both HONO and OH production from its photolysis. East China stations (TS, NUIST, LA, HNU, AHU, and CF) show similar peak times (12:00–14:00) but slightly lower magnitudes (1.0×10^{-4}–1.5×10^{-4} ppb·s^{-1}). In South China (GIG, SUST, GZ_ZL, GZ_NS, GZ_TM, GZ_GY, and GZ_DXC), peaks occur later (13:00–15:00) and are substantially higher (2.5×10^{-4}–5.5×10^{-4} ppb·s^{-1}), consistent with enhanced heterogeneous HONO formation under warm and humid conditions. Southwest China sites (CDAES and CQ) reach peak values of ~3.5×10^{-4} ppb·s^{-1}, comparable to those in South China, likely owing to basin-induced HONO accumulation and vigorous photochemistry. In Central China (LY), the peak (~2.7×10^{-4} ppb·s^{-1}) is similar to that in North and East China, indicating broadly comparable HONO sources and photolysis efficiencies across these regions.

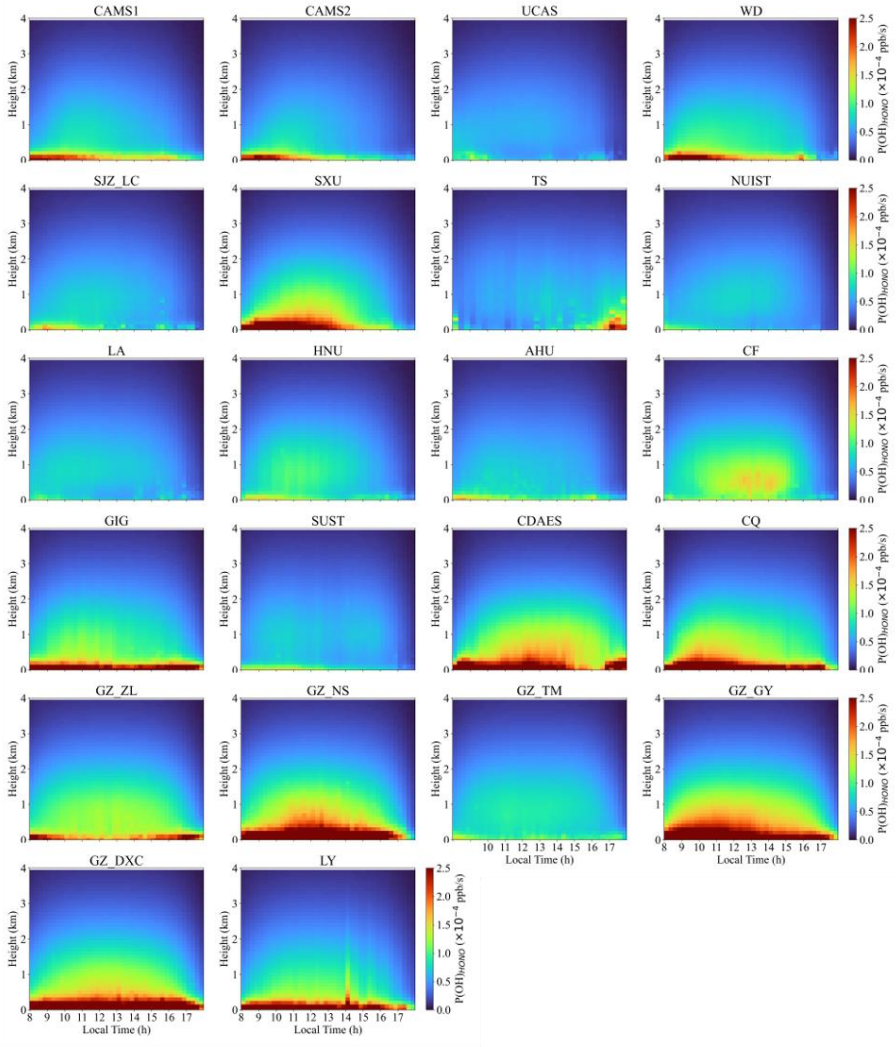

Figure 8. Mean vertical profiles of OH radicals generated by HONO photolysis.

Figure 9 presents the O_3 photolysis frequency, J($O(^1D)$), at all 22 sites follows a pronounced diurnal cycle, with maxima consistently occurring between 12:00 and 14:00 local time. Seasonal mean diurnal variations are presented in Figures S25–S28. In North China (CAMS1, CAMS2, UCAS, WD, SJZ_LC, and SXU), near-surface peak J($O(^1D)$) ranges from ~5×10^{-5} to 7×10^{-5} s^{-1}. The urban sites CAMS1, CAMS2, UCAS, and WD reach the highest values (~6×10^{-5}–7×10^{-5} s^{-1}) at midday. At SJZ_LC, located at the foothills of the Taihang Mountains, nocturnal temperature inversions can favor O_3 accumulation (Guo et al., 2024b; He et al., 2021), but the peak remains slightly lower (~5×10^{-5}–6×10^{-5} s^{-1}), likely constrained by local emissions. At the higher-altitude SXU site (780 m a.s.l.), near-surface J($O(^1D)$) is reduced (~4×10^{-5}–5×10^{-5} s^{-1}). Overall, urban stations exhibit larger J($O(^1D)$) than suburban and rural sites, reflecting higher O_3 levels driven by anthropogenic precursors and consistent with reported regional contrasts (Fardilah et al., 2023; Guo et al., 2024a; Qiu et al., 2025).In East China (TS, NUIST, LA, HNU, AHU, and CF), near-surface J($O(^1D)$) peaks at ~4×10^{-5}–6×10^{-5} s^{-1}, with urban sites such as NUIST and AHU reaching ~5×10^{-5}–6×10^{-5} s^{-1} at noon. In contrast, the high-altitude TS site (1500 m a.s.l.)

shows lower values (~3×10^{-5}–4×10^{-5} s^{-1}), consistent with its lower O_3 burden and cleaner background conditions. South China stations (GIG, SUST, GZ_ZL, GZ_NS, GZ_TM, GZ_GY, and GZ_DXC) display slightly higher peak J($O(^1D)$) (~6×10^{-5}–7×10^{-5} s^{-1}), in line with enhanced O_3 production under warm and humid subtropical conditions (Lu et al., 2025; Song et al., 2026; Zhang et al., 2025b). In Southwest China (CDAES and CQ), peak values (~5×10^{-5}–6×10^{-5} s^{-1}) are comparable to those in South China, likely driven by basin topography that favors O_3 accumulation and vigorous photochemistry (Qiao et al., 2019; Shu et al., 2023; Wang et al., 2024a). The Central China site LY exhibits slightly lower peaks (~4×10^{-5}–5×10^{-5} s^{-1}), similar to North and East China, indicating broadly comparable O_3 sources and photolysis efficiencies across these regions.

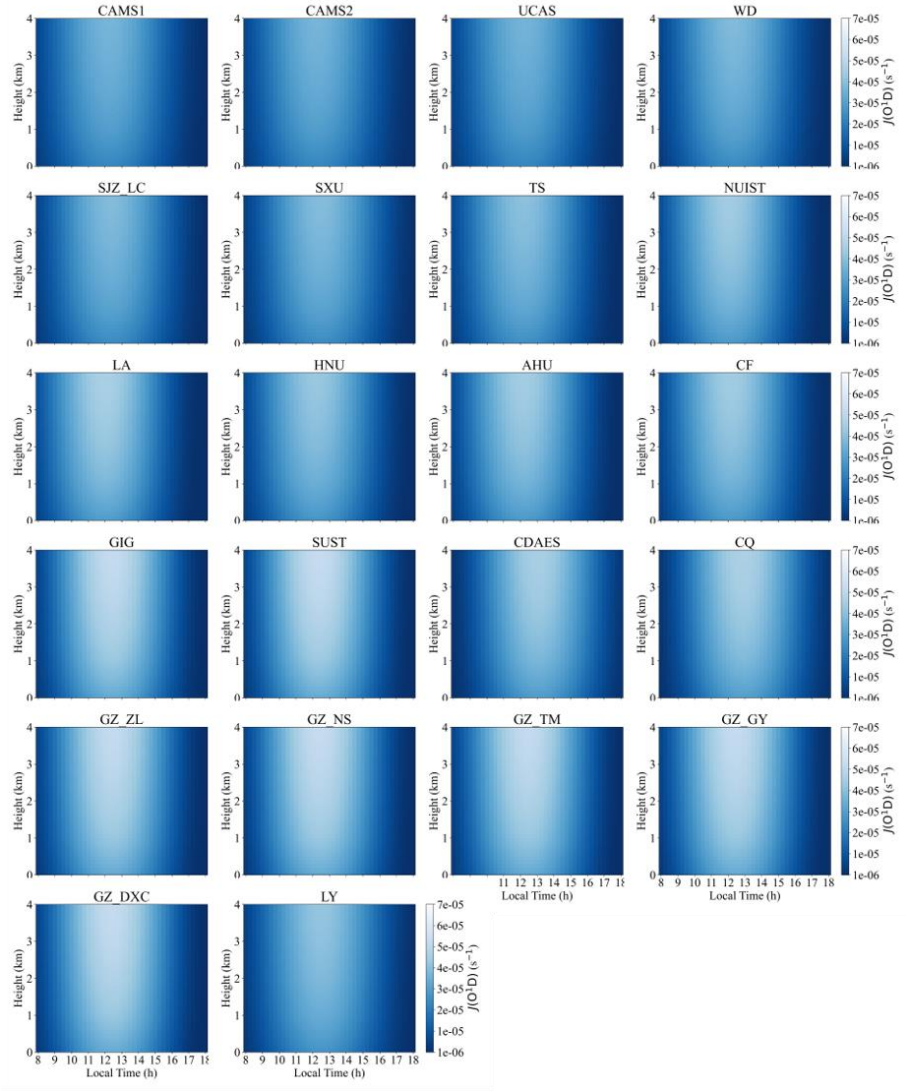

Figure 9. Mean diurnal vertical profiles of the O_3 photolysis rate, J($O(^1D)$).

Figure 10 presents the mean diurnal vertical profiles of the OH production rate from ozone photolysis, $P(OH)_{O3}$, at the 22 sites, and seasonal mean diurnal variations are presented in Figures S29–S32. All sites exhibit a pronounced unimodal diurnal cycle, with $P(OH)_{O3}$ increasing rapidly after sunrise, peaking between 12:00 and

14:00 local time, and declining thereafter. The vertical location of the maxima varies markedly among sites: at some, enhanced production is confined to the near-surface layer (0–0.5 km), whereas at others distinct maxima occur at 3–4 km, indicating substantial regional differences in photochemical regimes. Peak $P(OH)_{O3}$ spans 0.5×10^{-4}–2.0×10^{-4} ppb·s^{-1} across the network. In North China (CAMS1, CAMS2, UCAS, WD, SJZ_LC, and SXU), near-surface $P(OH)_{O3}$ during 12:00–14:00 reaches 1.0×10^{-4}–2.0×10^{-4} ppb·s^{-1}. The urban sites CAMS1, CAMS2, UCAS, and WD show the highest values (1.5×10^{-4}–2.0×10^{-4} ppb·s^{-1}), whereas SJZ_LC, likely influenced by local emissions and complex topography, exhibits slightly lower peaks (1.0×10^{-4}–1.5×10^{-4} ppb·s^{-1}). SXU reaches ~1.7×10^{-4} ppb·s^{-1}. At all these sites, $P(OH)_{O3}$ decreases with altitude and generally falls below 1.0×10^{-4} ppb·s^{-1} above 1 km. East China stations (TS, NUIST, LA, HNU, AHU, and CF) display similar peak timing (12:00–14:00), with near-surface maxima of 1.0×10^{-4}–1.8×10^{-4} ppb·s^{-1}. TS, NUIST, HNU, AHU, and CF reach ~1.5×10^{-4}–1.8×10^{-4} ppb·s^{-1}, while LA peaks at ~1.4×10^{-4} ppb·s^{-1}. In South China (GIG, SUST, GZ_ZL, GZ_NS, GZ_TM, GZ_GY, and GZ_DXC), the maxima occur slightly later (13:00–15:00) and are generally higher (1.3×10^{-4}–1.7×10^{-4} ppb·s^{-1}), with GZ_GY reaching ~1.9×10^{-4} ppb·s^{-1} and GZ_NS, GZ_TM, and GZ_DXC ~1.8×10^{-4} ppb·s^{-1}. Southwest China (CDAES and CQ) shows peaks of ~1.5×10^{-4}–2.5×10^{-4} ppb·s^{-1}, including ~1.9×10^{-4} ppb·s^{-1} at CQ and ~1.5×10^{-4} ppb·s^{-1} at CDAES. The Central China site LY exhibits a peak of ~1.5×10^{-4} ppb·s^{-1}, comparable to those in North and East China, indicating broadly similar ozone photochemical efficiencies across these regions.

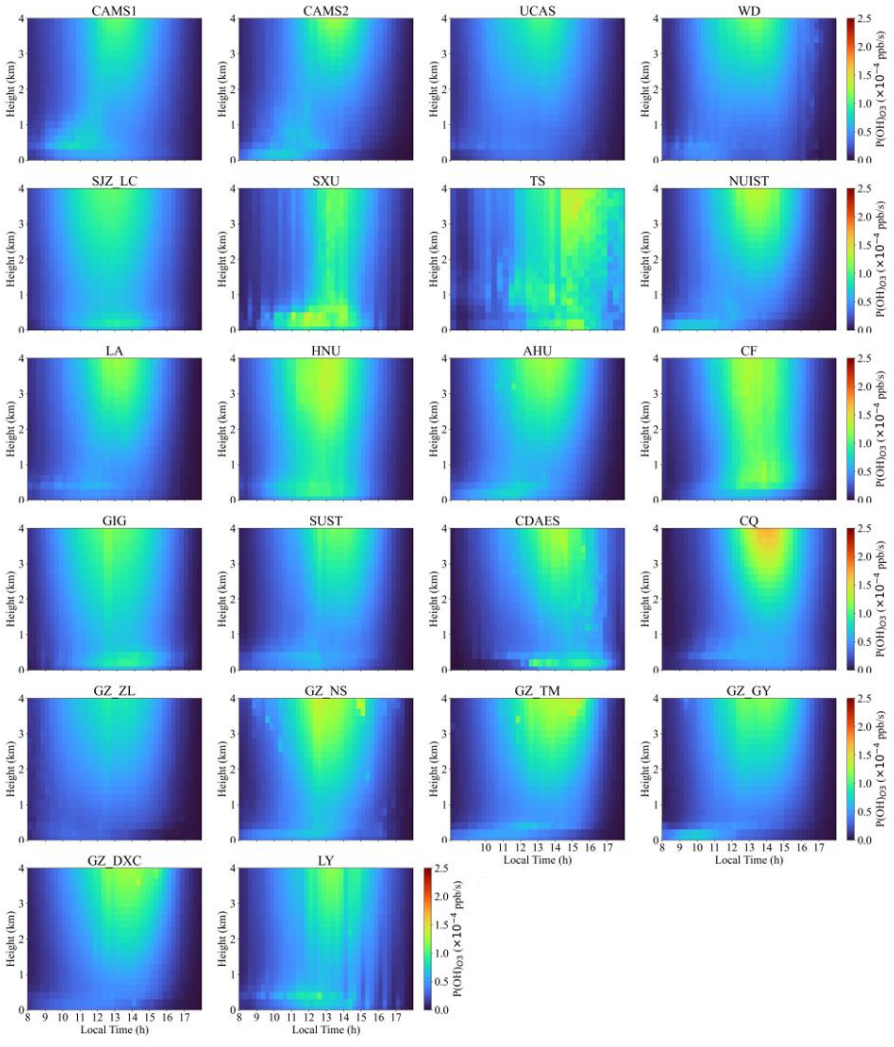

Figure 10. Mean vertical profiles of OH radicals produced by O_3 photolysis.

3.4 Validations with independent data

The dataset was validated using two independent approaches. First, O_3 VCD retrieved from the MAX-DOAS network for 2021–2024 were evaluated against coincident TROPOMI satellite observations. MAX-DOAS measurements were averaged within ±30 min of the TROPOMI overpass (13:30–14:00 Beijing Time), and TROPOMI pixels were spatially averaged over a 7 km × 5.5 km area center on each site, consistent with the native spatial resolution of TROPOMI. As shown in Figure 11a, the two datasets exhibit a strong linear relationship, with a Pearson correlation coefficient of R = 0.62 (N = 1897); site-resolved correlations are given in Figure 11c. Second, near-surface O_3 concentrations retrieved at the 22 hyperspectral sites were compared with in situ measurements from the nearest CNEMC over the same period. Site pairs were selected following the spatial representativeness criteria of Song et al. (2023b), Specifically, we prioritized the nearest CNEMC station within a maximum distance of ~10–15 km (detailed in Table S1) and verified environmental consistency between the paired sites using land-use and satellite-derived products, ensuring that

both sites sampled comparable urban or suburban atmospheric conditions. The comparison (Figure 11b) shows a significant positive correlation (R = 0.66, N = 9324), demonstrating good consistency between MAX-DOAS–derived surface O_3 and ground-based observations. The correlations for each hyperspectral site and its nearest CNEMC are summarized in Figure 11d. Together, these two independent validations demonstrate reasonable consistency and provide confidence in the dataset used in this study.

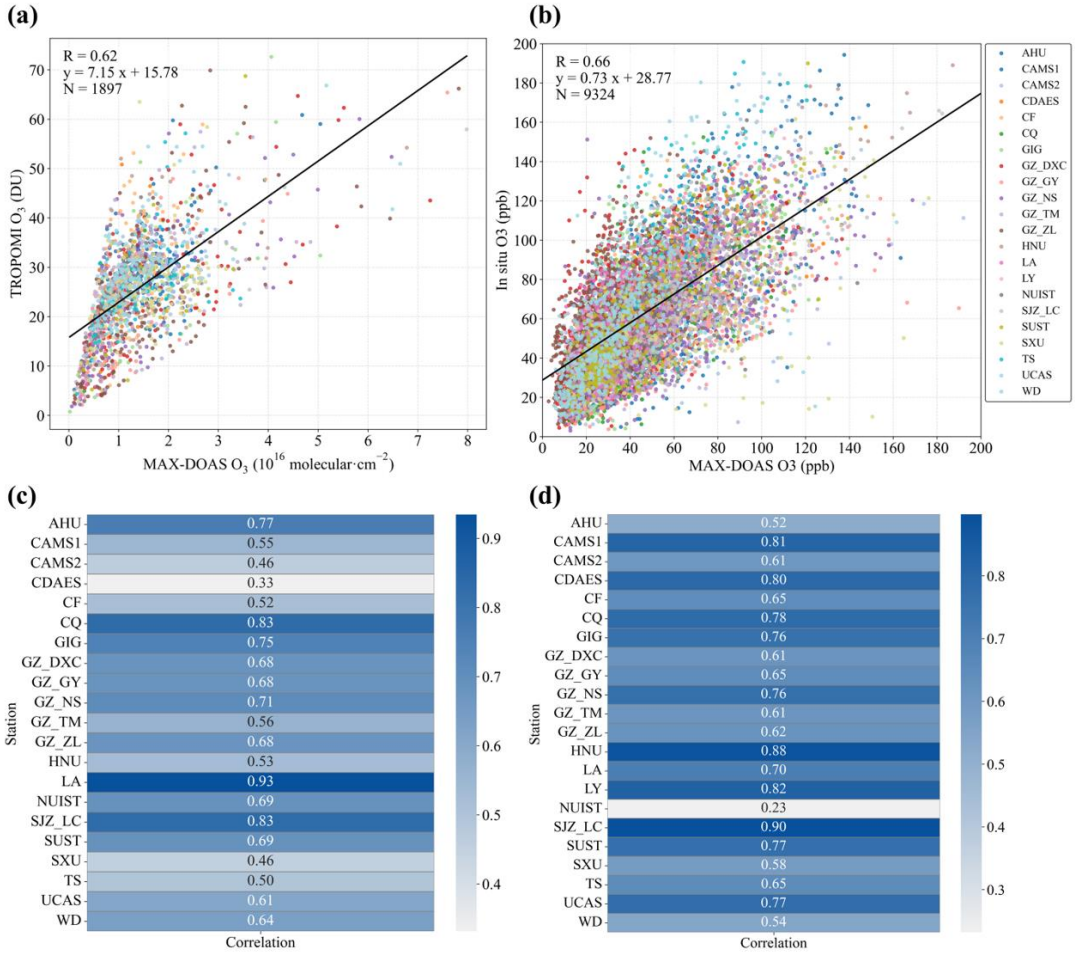

Figure 11. (a) Correlation between O_3 column densities retrieved from hyperspectral ground-based stations and TROPOMI satellite observations; (b) correlation between hyperspectral O_3 column densities and in situ O_3 measurements from the nearest CNEMC; (c) site-specific correlations between hyperspectral and TROPOMI O_3 column densities; (d) site-specific correlations between hyperspectral O_3 column densities and in situ O_3 at the nearest CNEMC.

4. Data availability

The vertical profiles of HONO and O_3, and the vertical profiles of OH radicals over the major regions of China presented in this study, are freely available in .xlsx format at Zenodo (https://doi.org/10.5281/zenodo.18489836; Zou et al., 2026).

5. Summary

We developed and released a comprehensive dataset of vertical profiles of HONO and O_3, and the associated OH radical production rates, $P(OH)_{HONO}$ and $P(OH)_{O3}$, derived from the Chinese hyperspectral vertical remote-sensing network for 2021–2024. The dataset spans 22 representative sites across North, East, Central, South, and Southwest China, covering a wide range of climatic regimes and surface types, and represents one of the most extensive publicly available collections in China in terms of spatial coverage and vertical resolution of photochemical parameters relevant to OH precursors. Independent validation against TROPOMI satellite retrievals and in situ measurements from the CNEMC demonstrates robust consistency. Mean diurnal profiles within 0–4 km reveal pronounced regional and vertical contrasts in HONO and O_3 driven photochemistry. Both J(HONO) and $J(O(^1D))$ exhibit radiation controlled, single-peaked diurnal cycles, with maxima around local noon (11:00–14:00), and remain elevated in the upper mixed layer and the lower free troposphere, reflecting the combined effects of radiative transfer and aerosol extinction on the vertical distribution of photolysis rates. Accordingly, $P(OH)_{HONO}$ and $P(OH)_{O3}$ peak near the surface and decrease with height, indicating that the boundary layer is the primary daytime source region of OH. At several plateau and mountainous sites, however, the lower free troposphere also shows a substantial radical production potential. Urban and highly industrialized sites exhibit higher photolysis rates and OH production, reflecting the combined effects of high precursor concentrations and strong radiation, while high-altitude clean-background sites, despite lower near-surface concentrations, maintain relatively large photolysis rates and significant OH production at middle and upper levels due to weaker aerosol extinction and stronger shortwave radiation, showing a vertical photochemical structure distinct from that over plains.

With continuous temporal coverage ranging from five months to 3.5 years and multi-site vertical profiling, this dataset provides a valuable foundation for: (1) quantifying the relative contributions of HONO and O_3 photolysis to the OH budget in the boundary layer and the lower free troposphere; (2) constraining radical initial conditions and radiative parameterizations in regional and global chemical transport models; (3) enabling cross-validation and synergistic inversion among ground-based, UAV, and satellite observations; (4) advancing studies of photochemical pollution formation, secondary aerosol production, and atmospheric oxidation capacity; and (5) supporting air-quality management and policy development as a complementary national monitoring resource. (6) serving as a critical benchmark for assessing and reducing uncertainties in vertical parameterization schemes (e.g., turbulent mixing, photolysis rates, heterogeneous reactions) within atmospheric chemical transport models. However, it is important to note the limitations of the current dataset. The time span (2021–2024) limits the capacity for robust analysis of long-term interannual trends driven by climate change or policy shifts. The observed photochemical regimes may not fully represent conditions during extreme climatic years outside this period,

and the climatological representativeness of sites with shorter operational histories requires continued data accumulation.

Declaration of competing interest

The authors declare that they have no known competing financial interests or personal relationships that could have appeared to influence the work reported in this paper.

Financial support

This work was supported by the National Natural Science Foundation of China (42588301, 42225504), the President's Foundation of Hefei Institutes of Physical Science, Chinese Academy of Sciences (YZJJQY202401, BJPY2024B09).

Author contributions

All authors contributed to the generation of the dataset described in this paper. Tiliang Zou, Chengzhi Xing, and Cheng Liu wrote the manuscript, while all other authors participated in its revision.

References

Aliwell, S. R., Van Roozendael, M., Johnston, P. V., Richter, A., Wagner, T., Arlander, D. W., Burrows, J. P., Fish, D. J., Jones, R. L., Tørnkvist, K. K., Lambert, J.-C., Pfeilsticker, K., and Pundt, I.: Analysis for BrO in zenith-sky spectra: An intercomparison exercise for analysis improvement, Journal of Geophysical Research: Atmospheres, 107, ACH 10-1-ACH 10-20, https://doi.org/10.1029/2001JD000329, 2002.

Ancellet, G., Viatte, C., Boynard, A., Ravetta, F., Pelon, J., Cailteau-Fischbach, C., Genau, P., Capo, J., Roy, A., and Nédélec, P.: Analysis of the day-to-day variability of ozone vertical profiles in the lower troposphere during the 2022 Paris ACROSS campaign, Atmospheric Chemistry and Physics, 24, 12963–12983, https://doi.org/10.5194/acp-24-12963-2024, 2024.

Andersen, S. T., Carpenter, L. J., Reed, C., Lee, J. D., Chance, R., Sherwen, T., Vaughan, A. R., Stewart, J., Edwards, P. M., Bloss, W. J., Sommariva, R., Crilley, L. R., Nott, G. J., Neves, L., Read, K., Heard, D. E., Seakins, P. W., Whalley, L. K., Boustead, G. A., Fleming, L. T., Stone, D., and Fomba, K. W.: Extensive field evidence for the release of HONO from the photolysis of nitrate aerosols, Science Advances, 9, eadd6266, https://doi.org/10.1126/sciadv.add6266, 2023.

Anon: Systematic Evaluation of Four Satellite AOD Datasets for Estimating PM2.5 Using a Random Forest Approach, Remote sensing, 15, 2064–2064, https://doi.org/10.3390/rs15082064, 2023.

Aumont, B., Chervier, F., and Laval, S.: Contribution of HONO sources to the

NOx/HOx/O3 chemistry in the polluted boundary layer, Atmospheric Environment, 37, 487–498, https://doi.org/10.1016/S1352-2310(02)00920-2, 2003.

Chambers, S. D., Guérette, E.-A., Monk, K., Griffiths, A. D., Zhang, Y., Duc, H., Cope, M., Emmerson, K. M., Chang, L. T., Silver, J. D., Utembe, S., Crawford, J., Williams, A. G., and Keywood, M.: Skill-Testing Chemical Transport Models across Contrasting Atmospheric Mixing States Using Radon-222, Atmosphere, 10, 25, https://doi.org/10.3390/atmos10010025, 2019.

Chen, Z., Xie, Y., Liu, J., Shen, L., Cheng, X., Han, H., Yang, M., Shen, Y., Zhao, T., and Hu, J.: Distinct seasonality in vertical variations of tropospheric ozone over coastal regions of southern China, Science of The Total Environment, 874, 162423, https://doi.org/10.1016/j.scitotenv.2023.162423, 2023.

Chen, Z., Liu, R., Wu, S., Xu, J., Wu, Y., and Qi, S.: Diurnal variation characteristics and meteorological causes of autumn ozone in the Pearl River Delta, China, Science of The Total Environment, 908, 168469, https://doi.org/10.1016/j.scitotenv.2023.168469, 2024.

Couillard, M. H., Schwab, M. J., Schwab, J. J., Lu, C.-H. (Sarah), Joseph, E., Stutsrim, B., Shrestha, B., Zhang, J., Knepp, T. N., and Gronoff, G. P.: Vertical Profiles of Ozone Concentrations in the Lower Troposphere Downwind of New York City During LISTOS 2018–2019, Journal of Geophysical Research: Atmospheres, 126, e2021JD035108, https://doi.org/10.1029/2021JD035108, 2021.

David, L. M. and Nair, P. R.: Diurnal and seasonal variability of surface ozone and NOx at a tropical coastal site: Association with mesoscale and synoptic meteorological conditions, Journal of Geophysical Research: Atmospheres, 116, https://doi.org/10.1029/2010JD015076, 2011.

Dewan, S. and Lakhani, A.: Tropospheric ozone and its natural precursors impacted by climatic changes in emission and dynamics, Front. Environ. Sci., 10, https://doi.org/10.3389/fenvs.2022.1007942, 2022.

Donzelli, G. and Suarez-Varela, M. M.: Tropospheric Ozone: A Critical Review of the Literature on Emissions, Exposure, and Health Effects, Atmosphere, 15, 779, https://doi.org/10.3390/atmos15070779, 2024.

Elshorbany, Y., Barnes, I., Becker, K., Kleffmann, J., and Wiesen, P.: Sources and cycling of tropospheric hydroxyl radicals - An overview, USF St. Petersburg Campus Faculty Publications, 2010.

Fardilah, R. D., Turyanti, A., Pangestu, L. A., Dominica, M. V., and Perdinan: Systematic Literature Review on Ozone Dispersion Correlated with Diurnal Concentration Pattern in Urban and Rural Areas, Agromet, 37, 77–90, https://doi.org/10.29244/j.agromet.37.2.77-90, 2023.

807 Fleischmann, O. C., Hartmann, M., Burrows, J. P., and Orphal, J.: New ultraviolet
808 absorption cross-sections of BrO at atmospheric temperatures measured by time-
809 windowing Fourier transform spectroscopy, Journal of Photochemistry and
810 Photobiology A: Chemistry, 168, 117–132,
811 https://doi.org/10.1016/j.jphotochem.2004.03.026, 2004.

812 Garcia-Nieto, D., Benavent, N., and Saiz-Lopez, A.: Measurements of atmospheric
813 HONO vertical distribution and temporal evolution in Madrid (Spain) using the
814 MAX-DOAS technique, Science of The Total Environment, 643, 957–966,
815 https://doi.org/10.1016/j.scitotenv.2018.06.180, 2018b.

816 Gu, R., Shen, H., Xue, L., Wang, T., Gao, J., Li, H., Liang, Y., Xia, M., Yu, C., Liu,
817 Y., and Wang, W.: Investigating the sources of atmospheric nitrous acid (HONO)
818 in the megacity of Beijing, China, Science of The Total Environment, 812,
819 152270, https://doi.org/10.1016/j.scitotenv.2021.152270, 2022.

820 Guo, J., Zhang, X., Gao, Y., Wang, Z., Zhang, M., Xue, W., Herrmann, H., Brasseur,
821 G. P., Wang, T., and Wang, Z.: Evolution of Ozone Pollution in China: What
822 Track Will It Follow?, Environ. Sci. Technol., 57, 109–117,
823 https://doi.org/10.1021/acs.est.2c08205, 2023.

824 Guo, P., Su, Y., Sun, X., Liu, C., Cui, B., Xu, X., Ouyang, Z., and Wang, X.: Urban–
825 Rural Comparisons of Biogenic Volatile Organic Compounds and Ground-Level
826 Ozone in Beijing, Forests, 15, 508, https://doi.org/10.3390/f15030508, 2024a.

827 Guo, W., Yang, Y., Zhang, J., Han, K., Yang, Y., Chen, Q., Li, S., and Zhu, Y.:
828 Effects of valley topography on ozone pollution in the Lanzhou valley: A
829 numerical case study, Environ Pollut, 363, 125225,
830 https://doi.org/10.1016/j.envpol.2024.125225, 2024b.

831 Hao, Q., Jiang, N., Zhang, R., Yang, L., and Li, S.: Characteristics, sources, and
832 reactions of nitrous acid during winter at an urban site in the Central Plains
833 Economic Region in China, Atmospheric Chemistry and Physics, 20, 7087–7102,
834 https://doi.org/10.5194/acp-20-7087-2020, 2020.

835 He, C., Wu, Q., Li, B., Liu, J., Gong, X., and Zhang, L.: Surface ozone pollution in
836 China: Trends, exposure risks, and drivers, Front. Public Health, 11,
837 https://doi.org/10.3389/fpubh.2023.1131753, 2023a.

838 He, G., He, C., Wang, H., Lu, X., Pei, C., Qiu, X., Liu, C., Wang, Y., Liu, N., Zhang,
839 J., Lei, L., Liu, Y., Wang, H., Deng, T., Fan, Q., and Fan, S.: Nighttime ozone in
840 the lower boundary layer: insights from 3-year tower-based measurements in
841 South China and regional air quality modeling, Atmospheric Chemistry and
842 Physics, 23, 13107–13124, https://doi.org/10.5194/acp-23-13107-2023, 2023b.

843 He, S., Wang, S., Zhang, S., Zhu, J., Sun, Z., Xue, R., and Zhou, B.: Vertical
844 distributions of atmospheric HONO and the corresponding OH radical

production by photolysis at the suburb area of Shanghai, China, Science of The Total Environment, 858, 159703, https://doi.org/10.1016/j.scitotenv.2022.159703, 2023c.

He, Y., Wang, H., Wang, H., Xu, X., Li, Y., and Fan, S.: Meteorology and topographic influences on nocturnal ozone increase during the summertime over Shaoguan, China, Atmospheric Environment, 256, 118459, https://doi.org/10.1016/j.atmosenv.2021.118459, 2021.

Hu, Q., Ji, X., Hong, Q., Li, J., Li, Q., Ou, J., Liu, H., Xing, C., Tan, W., Chen, J., Chang, B., and Liu, C.: Vertical Evolution of Ozone Formation Sensitivity Based on Synchronous Vertical Observations of Ozone and Proxies for Its Precursors: Implications for Ozone Pollution Prevention Strategies, Environ Sci Technol, 58, 4291–4301, https://doi.org/10.1021/acs.est.4c00637, 2024.

Itahashi, S., Mathur, R., Hogrefe, C., and Zhang, Y.: Modeling stratospheric intrusion and trans-Pacific transport on tropospheric ozone using hemispheric CMAQ during April 2010 – Part 1: Model evaluation and air mass characterization for stratosphere–troposphere transport, Atmospheric Chemistry and Physics, 20, 3373–3396, https://doi.org/10.5194/acp-20-3373-2020, 2020.

Ji, X., Liu, C., Wang, Y., Hu, Q., Lin, H., Zhao, F., Xing, C., Tang, G., Zhang, J., and Wagner, T.: Ozone profiles without blind area retrieved from MAX-DOAS measurements and comprehensive validation with multi-platform observations, Remote Sensing of Environment, 284, 113339, https://doi.org/10.1016/j.rse.2022.113339, 2023.

Johnson, M. S., Rozanov, A., Weber, M., Mettig, N., Sullivan, J., Newchurch, M. J., Kuang, S., Leblanc, T., Chouza, F., Berkoff, T. A., Gronoff, G., Strawbridge, K. B., Alvarez, R. J., Langford, A. O., Senff, C. J., Kirgis, G., McCarty, B., and Twigg, L.: TOLNet validation of satellite ozone profiles in the troposphere: impact of retrieval wavelengths, Atmospheric Measurement Techniques, 17, 2559–2582, https://doi.org/10.5194/amt-17-2559-2024, 2024.

Kim, H., Park, R. J., Hong, S.-Y., Park, D.-H., Kim, S.-W., Oak, Y. J., Feng, X., Lin, H., and Fu, T.-M.: A mixed layer height parameterization in a 3-D chemical transport model: Implications for gas and aerosol simulations, Sci Total Environ, 955, 176838, https://doi.org/10.1016/j.scitotenv.2024.176838, 2024.

Li, K., Jacob, D. J., Shen, L., Lu, X., De Smedt, I., and Liao, H.: Increases in surface ozone pollution in China from 2013 to 2019: anthropogenic and meteorological influences, Atmospheric Chemistry and Physics, 20, 11423–11433, https://doi.org/10.5194/acp-20-11423-2020, 2020.

Li, K., Tan, R., Qiao, W., Lee, T., Wang, Y., Zhang, D., Tang, M., Zhao, W., Gu, Y., Fan, S., Zhang, J., Lyu, X., Xue, L., Xu, J., Ma, Z., Latif, M. T., Amnuaylojaroen,

T., Gil, J., Lee, M.-H., Bak, J., Kim, J., Liao, H., Kanaya, Y., Lu, X., Nagashima, T., and Koo, J.-H.: Surface and tropospheric ozone over East Asia and Southeast Asia from observations: distributions, trends, and variability, Atmospheric Chemistry and Physics, 25, 11575–11596, https://doi.org/10.5194/acp-25-11575-2025, 2025a.

Li, M., McDonald, B. C., McKeen, S. A., Eskes, H., Levelt, P., Francoeur, C., Harkins, C., He, J., Barth, M., Henze, D. K., Bela, M. M., Trainer, M., de Gouw, J. A., and Frost, G. J.: Assessment of Updated Fuel-Based Emissions Inventories Over the Contiguous United States Using TROPOMI NO2 Retrievals, Journal of Geophysical Research: Atmospheres, 126, e2021JD035484, https://doi.org/10.1029/2021JD035484, 2021.

Li, Y., Xing, C., Peng, H., Jiao, P., Zhang, Q., Liu, C., Sun, Z., Tan, W., and Liu, C.: Vertical Differences in NO2-to-HONO Heterogeneous Conversion and HONO-Driven OH Production over Inland, Coastal, and Island Regions, Environ. Sci. Technol., 59, 26020–26030, https://doi.org/10.1021/acs.est.5c10318, 2025b.

Liang, Y., Zha, Q., Wang, W., Cui, L., Lui, K. H., Ho, K. F., Wang, Z., Lee, S., and Wang, T.: Revisiting nitrous acid (HONO) emission from on-road vehicles: A tunnel study with a mixed fleet, Journal of the Air & Waste Management Association, 67, 797–805, https://doi.org/10.1080/10962247.2017.1293573, 2017.

Liao, Z., Pan, Y., Ma, P., Jia, X., Cheng, Z., Wang, Q., Dou, Y., Zhao, X., Zhang, J., and Quan, J.: Meteorological and chemical controls on surface ozone diurnal variability in Beijing: A clustering-based perspective, Atmospheric Environment, 295, 119566, https://doi.org/10.1016/j.atmosenv.2022.119566, 2023.

Liao, Z., Gao, M., Zhang, J., Sun, J., Quan, J., Jia, X., Pan, Y., and Fan, S.: Mixing-layer-height-referenced ozone vertical distribution in the lower troposphere of Chinese megacities: stratification, classification, and meteorological and photochemical mechanisms, Atmospheric Chemistry and Physics, 24, 3541–3557, https://doi.org/10.5194/acp-24-3541-2024, 2024.

Liao, Z., Zhang, J., Gao, M., and Ma, Z.: Widespread stratospheric intrusion influence on summer ozone pollution over China revealed by multi-site ozonesonde and validated EAC4 reanalysis, Atmospheric Chemistry and Physics, 25, 14865–14877, https://doi.org/10.5194/acp-25-14865-2025, 2025.

Lin, H., Xing, C., Hong, Q., Liu, C., Ji, X., Liu, T., Lin, J., Lu, C., Tan, W., Li, Q., and Liu, H.: Diagnosis of Ozone Formation Sensitivities in Different Height Layers via MAX-DOAS Observations in Guangzhou, Journal of Geophysical Research: Atmospheres, 127, e2022JD036803, https://doi.org/10.1029/2022JD036803, 2022.

Liu, C., Xing, C., Hu, Q., Li, Q., Liu, H., Hong, Q., Tan, W., Ji, X., Lin, H., Lu, C., Lin, J., Liu, H., Wei, S., Chen, J., Yang, K., Wang, S., Liu, T., and Chen, Y.: Ground-Based Hyperspectral Stereoscopic Remote Sensing Network: A Promising Strategy to Learn Coordinated Control of O3 and PM2.5 over China, Engineering, 19, 71–83, https://doi.org/10.1016/j.eng.2021.02.019, 2022a.

Liu, H., Han, X., Tang, G., Zhang, J., Xia, X., Zhang, M., and Meng, L.: Model analysis of vertical exchange of boundary layer ozone and its impact on surface air quality over the North China Plain, Science of The Total Environment, 821, 153436, https://doi.org/10.1016/j.scitotenv.2022.153436, 2022b.

Liu, P., Xue, C., Ye, C., Liu, C., Zhang, C., Wang, J., Zhang, Y., Liu, J., and Mu, Y.: The Lack of HONO Measurement May Affect the Accurate Diagnosis of Ozone Production Sensitivity, ACS Environ. Au, 3, 18–23, https://doi.org/10.1021/acsenvironau.2c00048, 2023a.

Liu, X., Yi, G., Zhou, X., Zhang, T., Bie, X., Li, J., and Tan, H.: Spatio-temporal variations of PM2.5 and O3 in China during 2013–2021: Impact factor analysis, Environmental Pollution, 334, 122189, https://doi.org/10.1016/j.envpol.2023.122189, 2023b.

Lu, Y., Kong, L., Shen, J., Liu, B., An, Y., Wang, Y., Tan, J., and Wang, L.: Characteristics and influencing factors of ambient ozone pollution in Hangzhou in the relative humidity range with high ozone levels, Atmospheric Pollution Research, 16, 102648, https://doi.org/10.1016/j.apr.2025.102648, 2025.

Lyu, Y., Xu, H., Wu, H., Han, F., Lv, F., Kang, A., and Pang, X.: Spatiotemporal variations of PM2.5 and ozone in urban agglomerations of China and meteorological drivers for ozone using explainable machine learning, Environmental Pollution, 365, 125380, https://doi.org/10.1016/j.envpol.2024.125380, 2025.

Meng, F., Qin, M., Tang, K., Duan, J., Fang, W., Liang, S., Ye, K., Xie, P., Sun, Y., Xie, C., Ye, C., Fu, P., Liu, J., and Liu, W.: High-resolution vertical distribution and sources of HONO and NO_2 in the nocturnal boundary layer in urban Beijing, China, Atmospheric Chemistry and Physics, 20, 5071–5092, https://doi.org/10.5194/acp-20-5071-2020, 2020.

Monks, P. S., Archibald, A. T., Colette, A., Cooper, O., Coyle, M., Derwent, R., Fowler, D., Granier, C., Law, K. S., Mills, G. E., Stevenson, D. S., Tarasova, O., Thouret, V., von Schneidemesser, E., Sommariva, R., Wild, O., and Williams, M. L.: Tropospheric ozone and its precursors from the urban to the global scale from air quality to short-lived climate forcer, Atmospheric Chemistry and Physics, 15, 8889–8973, https://doi.org/10.5194/acp-15-8889-2015, 2015.

Orphal, J. and Chance, K.: Ultraviolet and visible absorption cross-sections for

959 HITRAN, Journal of Quantitative Spectroscopy and Radiative Transfer, 82, 491–
960 504, https://doi.org/10.1016/S0022-4073(03)00173-0, 2003.

961 Park, S., Son, S.-W., Jung, M.-I., Park, J., and Park, S. S.: Evaluation of tropospheric
962 ozone reanalyses with independent ozonesonde observations in East Asia, Geosci.
963 Lett., 7, 12, https://doi.org/10.1186/s40562-020-00161-9, 2020.

964 Qiao, X., Guo, H., Wang, P., Tang, Y., Ying, Q., Zhao, X., Deng, W., and Zhang, H.:
965 Fine Particulate Matter and Ozone Pollution in the 18 Cities of the Sichuan Basin
966 in Southwestern China: Model Performance and Characteristics, Aerosol Air
967 Qual. Res., 19, 2308–2319, https://doi.org/10.4209/aaqr.2019.05.0235, 2019.

968 Qiu, Y., Li, X., Chai, W., Liu, Y., Song, M., Tian, X., Zou, Q., Lou, W., Zhang, W.,
969 Li, J., and Zhang, Y.: Insights into ozone pollution control in urban areas by
970 decoupling meteorological factors based on machine learning, Atmospheric
971 Chemistry and Physics, 25, 1749–1763, https://doi.org/10.5194/acp-25-1749-
972 2025, 2025.

973 Qu, H., Wang, Y., Zhang, R., and Li, J.: Extending Ozone-Precursor Relationships in
974 China From Peak Concentration to Peak Time, Journal of Geophysical Research:
975 Atmospheres, 125, e2020JD033670, https://doi.org/10.1029/2020JD033670,
976 2020.

977 R. Crilley, L., Kramer, L., D. Pope, F., K. Whalley, L., R. Cryer, D., E. Heard, D.,
978 D. Lee, J., Reed, C., and J. Bloss, W.: On the interpretation of in situ HONO
979 observations via photochemical steady state, Faraday Discussions, 189, 191–212,
980 https://doi.org/10.1039/C5FD00224A, 2016.

981 Ryan, R. G., Rhodes, S., Tully, M., Wilson, S., Jones, N., Frieß, U., and Schofield, R.:
982 Daytime HONO, NO_2 and aerosol distributions from MAX-DOAS observations
983 in Melbourne, Atmospheric Chemistry and Physics, 18, 13969–13985,
984 https://doi.org/10.5194/acp-18-13969-2018, 2018a.

985 Sekiya, T., Emili, E., Miyazaki, K., Inness, A., Qu, Z., Pierce, R. B., Jones, D.,
986 Worden, H., Cheng, W. Y. Y., Huijnen, V., and Koren, G.: Assessing the relative
987 impacts of satellite ozone and its precursor observations to improve global
988 tropospheric ozone analysis using multiple chemical reanalysis systems,
989 Atmospheric Chemistry and Physics, 25, 2243–2268,
990 https://doi.org/10.5194/acp-25-2243-2025, 2025.

991 Serdyuchenko, A., Gorshelev, V., Weber, M., Chehade, W., and Burrows, J. P.: High
992 spectral resolution ozone absorption cross-sections – Part 2: Temperature
993 dependence, Atmospheric Measurement Techniques, 7, 625–636,
994 https://doi.org/10.5194/amt-7-625-2014, 2014.

995 Sharma, B. R., Kuttippurath, J., and Gopikrishnan, G. S.: Tropospheric ozone as an
996 atmospheric pollutant and short-lived climate forcer in the Third Pole,

997 Chemosphere, 380, 144474, https://doi.org/10.1016/j.chemosphere.2025.144474,
998 2025.

999 Shi, Y., Zeng, Q., Liu, L., Huo, J., Zhang, Z., Ding, W., and Hu, F.: Observed
1000 Evidence That Subsidence Process Stabilizes the Boundary Layer and Increases
1001 the Ground Concentration of Secondary Pollutants, Journal of Geophysical
1002 Research: Atmospheres, 127, e2021JD035244,
1003 https://doi.org/10.1029/2021JD035244, 2022.

1004 Shu, Z., Zhao, T., Chen, Y., Liu, Y., Yang, F., Jiang, Y., He, G., Yang, Q., and Zhang,
1005 Y.: Terrain effect on atmospheric process in seasonal ozone variation over the
1006 Sichuan Basin, Southwest China, Environmental Pollution, 338, 122622,
1007 https://doi.org/10.1016/j.envpol.2023.122622, 2023.

1008 Song, M., Zhao, X., Liu, P., Mu, J., He, G., Zhang, C., Tong, S., Xue, C., Zhao, X.,
1009 Ge, M., and Mu, Y.: Atmospheric NOx oxidation as major sources for nitrous
1010 acid (HONO), npj Clim Atmos Sci, 6, 30, https://doi.org/10.1038/s41612-023-
1011 00357-8, 2023a.

1012 Song, X., Li, X.-B., Yuan, B., He, X., Chen, Y., Wang, S., Huangfu, Y., Peng, Y.,
1013 Zhang, C., Liu, A., Yang, H., Liu, C., Li, J., and Shao, M.: Elucidating key
1014 factors in regulating budgets of ozone and its precursors in atmospheric
1015 boundary layer, npj Clim Atmos Sci, 7, 262, https://doi.org/10.1038/s41612-024-
1016 00818-8, 2024.

1017 Song, Y., Xing, C., Liu, C., Lin, J., Wu, H., Liu, T., Lin, H., Zhang, C., Tan, W., Ji,
1018 X., Liu, H., and Li, Q.: Evaluation of transport processes over North China Plain
1019 and Yangtze River Delta using MAX-DOAS observations, Atmospheric
1020 Chemistry and Physics, 23, 1803–1824, https://doi.org/10.5194/acp-23-1803-
1021 2023, 2023b.

1022 Song, Y., Wang, P., Yang, Y., Tang, J., and Liao, H.: Meteorological conditions and
1023 physicochemical processes amplifying ozone pollution during heatwaves in
1024 major city clusters of China, Atmospheric Research, 330, 108580,
1025 https://doi.org/10.1016/j.atmosres.2025.108580, 2026.

1026 Spataro, F. and Ianniello, A.: Sources of atmospheric nitrous acid: State of the science,
1027 current research needs, and future prospects, Journal of the Air & Waste
1028 Management Association, 64, 1232–1250,
1029 https://doi.org/10.1080/10962247.2014.952846, 2014.

1030 Spurr, R. J. D.: VLIDORT: A linearized pseudo-spherical vector discrete ordinate
1031 radiative transfer code for forward model and retrieval studies in multilayer
1032 multiple scattering media, Journal of Quantitative Spectroscopy and Radiative
1033 Transfer, 102, 316–342, https://doi.org/10.1016/j.jqsrt.2006.05.005, 2006.

1034 Stutz, J., Kim, E. S., Platt, U., Bruno, P., Perrino, C., and Febo, A.: UV-visible

absorption cross sections of nitrous acid, Journal of Geophysical Research: Atmospheres, 105, 14585–14592, https://doi.org/10.1029/2000JD900003, 2000.

Su, W., Liu, C., Hu, Q., Fan, G., Xie, Z., Huang, X., Zhang, T., Chen, Z., Dong, Y., Ji, X., Liu, H., Wang, Z., and Liu, J.: Characterization of ozone in the lower troposphere during the 2016 G20 conference in Hangzhou, Sci Rep, 7, 17368, https://doi.org/10.1038/s41598-017-17646-x, 2017.

Tang, Y., An, J., Wang, F., Li, Y., Qu, Y., Chen, Y., and Lin, J.: Impacts of an unknown daytime HONO source on the mixing ratio and budget of HONO, and hydroxyl, hydroperoxyl, and organic peroxy radicals, in the coastal regions of China, Atmospheric Chemistry and Physics, 15, 9381–9398, https://doi.org/10.5194/acp-15-9381-2015, 2015.

Thalman, R. and Volkamer, R.: Temperature dependent absorption cross-sections of O2–O2 collision pairs between 340 and 630 nm and at atmospherically relevant pressure, Phys. Chem. Chem. Phys., 15, 15371, https://doi.org/10.1039/c3cp50968k, 2013.

Thürkow, M., Schaap, M., Kranenburg, R., Pfäfflin, F., Neunhäuserer, L., Wolke, R., Heinold, B., Stoll, J., Lupaşcu, A., Nordmann, S., Minkos, A., and Butler, T.: Dynamic evaluation of modeled ozone concentrations in Germany with four chemistry transport models, Science of The Total Environment, 906, 167665, https://doi.org/10.1016/j.scitotenv.2023.167665, 2024.

Torres, O., Jethva, H., Ahn, C., Jaross, G., and Loyola, D. G.: TROPOMI aerosol products: evaluation and observations of synoptic-scale carbonaceous aerosol plumes during 2018–2020, Atmospheric Measurement Techniques, 13, 6789–6806, https://doi.org/10.5194/amt-13-6789-2020, 2020b.

Vandaele, A. C., Hermans, C., Simon, P. C., Carleer, M., Colin, R., Fally, S., Mérienne, M. F., Jenouvrier, A., and Coquart, B.: Measurements of the NO2 absorption cross-section from 42 000 cm−1 to 10 000 cm−1 (238–1000 nm) at 220 K and 294 K, Journal of Quantitative Spectroscopy and Radiative Transfer, 59, 171–184, https://doi.org/10.1016/S0022-4073(97)00168-4, 1998.

Wang, N., Du, Y., Chen, D., Meng, H., Chen, X., Zhou, L., Shi, G., Zhan, Y., Feng, M., Li, W., Chen, M., Li, Z., and Yang, F.: Spatial disparities of ozone pollution in the Sichuan Basin spurred by extreme, hot weather, Atmospheric Chemistry and Physics, 24, 3029–3042, https://doi.org/10.5194/acp-24-3029-2024, 2024a.

Wang, R., Shen, H., Zeng, C., Chen, J., Wang, Y., and Li, Y.: A global land daily 10-km-resolution surface ozone dataset from 2013–2022, Sci Data, 12, 1710, https://doi.org/10.1038/s41597-025-05990-x, 2025a.

Wang, W.-N., Cheng, T.-H., Gu, X.-F., Chen, H., Guo, H., Wang, Y., Bao, F.-W., Shi, S.-Y., Xu, B.-R., Zuo, X., Meng, C., and Zhang, X.-C.: Assessing Spatial and

Temporal Patterns of Observed Ground-level Ozone in China, Sci Rep, 7, 3651, https://doi.org/10.1038/s41598-017-03929-w, 2017.

Wang, X., Zhang, H., Hong, X., Xiang, Y., Wang, S., Zhang, T., Qin, Z., and Ou, J.: Vertical profiles and regional transport of ozone in typical area of Yangtze-Huaihe River Basin during the autumn base on multiple lidars, Atmospheric Pollution Research, 15, 101983, https://doi.org/10.1016/j.apr.2023.101983, 2024b.

Wang, Y., Puķīte, J., Wagner, T., Donner, S., Beirle, S., Hilboll, A., Vrekoussis, M., Richter, A., Apituley, A., Piters, A., Allaart, M., Eskes, H., Frumau, A., Van Roozendael, M., Lampel, J., Platt, U., Schmitt, S., Swart, D., and Vonk, J.: Vertical Profiles of Tropospheric Ozone From MAX-DOAS Measurements During the CINDI-2 Campaign: Part 1—Development of a New Retrieval Algorithm, Journal of Geophysical Research: Atmospheres, 123, 10,637-10,670, https://doi.org/10.1029/2018JD028647, 2018.

Wang, Y., Dörner, S., Donner, S., Böhnke, S., De Smedt, I., Dickerson, R. R., Dong, Z., He, H., Li, Z., Li, Z., Li, D., Liu, D., Ren, X., Theys, N., Wang, Y., Wang, Y., Wang, Z., Xu, H., Xu, J., and Wagner, T.: Vertical profiles of NO_2, SO_2, HONO, HCHO, CHOCHO and aerosols derived from MAX-DOAS measurements at a rural site in the central western North China Plain and their relation to emission sources and effects of regional transport, Atmospheric Chemistry and Physics, 19, 5417–5449, https://doi.org/10.5194/acp-19-5417-2019, 2019.

Wang, Y., Gao, W., Wang, S., Song, T., Gong, Z., Ji, D., Wang, L., Liu, Z., Tang, G., Huo, Y., Tian, S., Li, J., Li, M., Yang, Y., Chu, B., Petäjä, T., Kerminen, V.-M., He, H., Hao, J., Kulmala, M., Wang, Y., and Zhang, Y.: Contrasting trends of PM2.5 and surface-ozone concentrations in China from 2013 to 2017, Natl Sci Rev, 7, 1331–1339, https://doi.org/10.1093/nsr/nwaa032, 2020.

Wang, Y., Yang, Y., Yuan, Q., Li, T., Zhou, Y., Zong, L., Wang, M., Xie, Z., Ho, H. C., Gao, M., Tong, S., Lolli, S., and Zhang, L.: Substantially underestimated global health risks of current ozone pollution, Nat Commun, 16, 102, https://doi.org/10.1038/s41467-024-55450-0, 2025b.

Wang, Z., Zhang, H., Shi, C., Ji, X., Zhu, Y., Xia, C., Sun, X., Zhang, M., Lin, X., Yan, S., Zhou, Y., Xing, C., Chen, Y., and Liu, C.: Vertical and spatial differences in ozone formation sensitivities under different ozone pollution levels in eastern Chinese cities, npj Clim Atmos Sci, 8, 30, https://doi.org/10.1038/s41612-024-00855-3, 2025c.

Xia, N., Du, E., Guo, Z., and de Vries, W.: The diurnal cycle of summer tropospheric ozone concentrations across Chinese cities: Spatial patterns and main drivers, Environmental Pollution, 286, 117547, https://doi.org/10.1016/j.envpol.2021.117547, 2021.

Xing, C., Liu, C., Wang, S., Chan, K. L., Gao, Y., Huang, X., Su, W., Zhang, C., Dong, Y., Fan, G., Zhang, T., Chen, Z., Hu, Q., Su, H., Xie, Z., and Liu, J.: Observations of the vertical distributions of summertime atmospheric pollutants and the corresponding ozone production in Shanghai, China, Atmospheric Chemistry and Physics, 17, 14275–14289, https://doi.org/10.5194/acp-17-14275-2017, 2017.

Xing, C., Liu, C., Wang, S., Hu, Q., Liu, H., Tan, W., Zhang, W., Li, B., and Liu, J.: A new method to determine the aerosol optical properties from multiple-wavelength O_4 absorptions by MAX-DOAS observation, Atmospheric Measurement Techniques, 12, 3289–3302, https://doi.org/10.5194/amt-12-3289-2019, 2019.

Xing, C., Liu, C., Wu, H., Lin, J., Wang, F., Wang, S., and Gao, M.: Ground-based vertical profile observations of atmospheric composition on the Tibetan Plateau (2017–2019), Earth System Science Data, 13, 4897–4912, https://doi.org/10.5194/essd-13-4897-2021, 2021a.

Xing, C., Liu, C., Hu, Q., Fu, Q., Wang, S., Lin, H., Zhu, Y., Wang, S., Wang, W., Javed, Z., Ji, X., and Liu, J.: Vertical distributions of wintertime atmospheric nitrogenous compounds and the corresponding OH radicals production in Leshan, southwest China, Journal of Environmental Sciences, 105, 44–55, https://doi.org/10.1016/j.jes.2020.11.019, 2021b.

Xing, C., Liu, C., Hong, Q., Liu, H., Wu, H., Lin, J., Song, Y., Chen, Y., Liu, T., Hu, Q., Tan, W., and Lin, H.: Vertical distributions and potential sources of wintertime atmospheric pollutants and the corresponding ozone production on the coast of Bohai Sea, Journal of Environmental Management, 319, 115721, https://doi.org/10.1016/j.jenvman.2022.115721, 2022.

Xing, C., Xu, S., Song, Y., Liu, C., Liu, Y., Lu, K., Tan, W., Zhang, C., Hu, Q., Wang, S., Wu, H., and Lin, H.: A new insight into the vertical differences in NO_2 heterogeneous reaction to produce HONO over inland and marginal seas, Atmospheric Chemistry and Physics, 23, 5815–5834, https://doi.org/10.5194/acp-23-5815-2023, 2023.

Xing, C., Liu, C., Li, Q., Wang, S., Tan, W., Zou, T., Wang, Z., and Lu, C.: Observations of HONO and its precursors between urban and its surrounding agricultural fields: The vertical transports, sources and contribution to OH, Science of The Total Environment, 915, 169159, https://doi.org/10.1016/j.scitotenv.2023.169159, 2024a.

Xing, C., Liu, C., Ye, C., Xue, J., Wu, H., Ji, X., Ou, J., and Hu, Q.: Observations of the vertical distributions of summertime atmospheric pollutants in Nam Co: OH production and source analysis, Atmospheric Chemistry and Physics, 24, 10093–10112, https://doi.org/10.5194/acp-24-10093-2024, 2024c.

Xu, S., Wang, S., Xia, M., Lin, H., Xing, C., Ji, X., Su, W., Tan, W., Liu, C., and Hu, Q.: Observations by Ground-Based MAX-DOAS of the Vertical Characters of Winter Pollution and the Influencing Factors of HONO Generation in Shanghai, China, Remote Sensing, 13, 3518, https://doi.org/10.3390/rs13173518, 2021.

Xuan, H., Liu, J., Zhao, Y., Cao, Q., Chen, T., Wang, Y., Liu, Z., Sun, X., Li, H., Zhang, P., Chu, B., Ma, Q., and He, H.: Relative humidity driven nocturnal HONO formation mechanism in autumn haze events of Beijing, npj Clim Atmos Sci, 7, 193, https://doi.org/10.1038/s41612-024-00745-8, 2024.

Xuan, H., Lian, C., Ma, P., Lan, L., Wang, W., Liu, C., Quan, J., Zhang, S., Liu, J., Li, H., Chen, T., Zhang, P., Wang, Y., Chu, B., Ma, Q., and He, H.: Vertical Distribution of Sources and Atmospheric Impacts of HONO in the North China Plain, Environ. Sci. Technol., 59, 17666–17676, https://doi.org/10.1021/acs.est.5c01801, 2025b.

Xue, C., Ye, C., Zhang, C., Catoire, V., and Mu, Y.: Evidence for Strong HONO Emission from Fertilized Agricultural Fields and its Remarkable Impact on Regional O 3 Pollution in the Summer North China Plain, ACS Earth and Space Chemistry, 5, https://doi.org/10.1021/acsearthspacechem.0c00314, 2021.

Xue, C., Chen, H., McGillen, M. R., Su, H., Cheng, Y., Kleffmann, J., Li, G., Cazaunau, M., Colomb, A., Sciare, J., DeWitt, L., Marchand, N., Sarda-Esteve, R., Petit, J.-E., and Kukui, A.: Role of Heterogeneous Reactions in the Atmospheric Oxidizing Capacity in Island Environments, Environ. Sci. Technol., 59, 3153–3164, https://doi.org/10.1021/acs.est.4c11647, 2025.

Yang, G., Liu, Y., and Li, X.: Spatiotemporal distribution of ground-level ozone in China at a city level, Sci Rep, 10, 7229, https://doi.org/10.1038/s41598-020-64111-3, 2020.

Ye, C., Lu, K., Ma, X., Qiu, W., Li, S., Yang, X., Xue, C., Zhai, T., Liu, Y., Li, X., Li, Y., Wang, H., Tan, Z., Chen, X., Dong, H., Zeng, L., Hu, M., and Zhang, Y.: HONO chemistry at a suburban site during the EXPLORE-YRD campaign in 2018: formation mechanisms and impacts on O_3 production, Atmospheric Chemistry and Physics, 23, 15455–15472, https://doi.org/10.5194/acp-23-15455-2023, 2023a.

Ye, C., Lu, K., Ma, X., Qiu, W., Li, S., Yang, X., Xue, C., Zhai, T., Liu, Y., Li, X., Li, Y., Wang, H., Tan, Z., Chen, X., Dong, H., Zeng, L., Hu, M., and Zhang, Y.: HONO chemistry at a suburban site during the EXPLORE-YRD campaign in 2018: formation mechanisms and impacts on O_3 production, Atmospheric Chemistry and Physics, 23, 15455–15472, https://doi.org/10.5194/acp-23-15455-2023, 2023b.

Yu, H., De Smedt, I., Theys, N., Sneep, M., Veefkind, P., and Van Roozendael, M.:

Harmonized cloud datasets for the Ozone Monitoring Instrument (OMI) and TROPOspheric Monitoring Instrument (TROPOMI) using the O_2–O_2 477 nm absorption band, Atmospheric Measurement Techniques, 18, 4131–4163, https://doi.org/10.5194/amt-18-4131-2025, 2025.

Yu, Y., Cheng, P., Li, H., Yang, W., Han, B., Song, W., Hu, W., Wang, X., Yuan, B., Shao, M., Huang, Z., Li, Z., Zheng, J., Wang, H., and Yu, X.: Budget of nitrous acid (HONO) at an urban site in the fall season of Guangzhou, China, Atmospheric Chemistry and Physics, 22, 8951–8971, https://doi.org/10.5194/acp-22-8951-2022, 2022.

Zeng, Y., Zhang, J., Li, D., Liao, Z., Bian, J., Bai, Z., Shi, H., Xuan, Y., Yao, Z., and Chen, H.: Vertical distribution of tropospheric ozone and its sources of precursors over Beijing: Results from ~ 20 years of ozonesonde measurements based on clustering analysis, Atmospheric Research, 284, 106610, https://doi.org/10.1016/j.atmosres.2023.106610, 2023.

Zhang, H., Ren, C., Zhou, X., Tang, K., Liu, Y., Liu, T., Wang, J., Chi, X., Li, M., Li, N., Huang, X., and Ding, A.: Improving HONO Simulations and Evaluating Its Impacts on Secondary Pollution in the Yangtze River Delta Region, China, Journal of Geophysical Research: Atmospheres, 129, e2024JD041052, https://doi.org/10.1029/2024JD041052, 2024.

Zhang, H., Shi, C., Ying, C., Weng, S., Ni, E., Zhao, L., Yang, P., Tang, K., Zhou, X., Ren, C., Chi, X., Zhou, D., Li, M., Li, N., Liu, T., and Huang, X.: HONO formation mechanisms and impacts on ambient oxidants in coastal regions of Fujian, China, Atmospheric Chemistry and Physics, 25, 16797–16816, https://doi.org/10.5194/acp-25-16797-2025, 2025a.

Zhang, Q., Liu, P., Wang, Y., George, C., Chen, T., Ma, S., Ren, Y., Mu, Y., Song, M., Herrmann, H., Mellouki, A., Chen, J., Yue, Y., Zhao, X., Wang, S., and Zeng, Y.: Unveiling the underestimated direct emissions of nitrous acid (HONO), Proc Natl Acad Sci U S A, 120, e2302048120, https://doi.org/10.1073/pnas.2302048120, 2023a.

Zhang, X., Tong, S., Jia, C., Zhang, W., Wang, Z., Tang, G., Hu, B., Liu, Z., Wang, L., Zhao, P., Pan, Y., and Ge, M.: Elucidating HONO formation mechanism and its essential contribution to OH during haze events, npj Clim Atmos Sci, 6, 55, https://doi.org/10.1038/s41612-023-00371-w, 2023b.

Zhang, X., Yan, Y., Zhang, N., Wang, W., Suo, H., Jian, X., Wang, C., Ma, H., Gao, H., Yang, Z., Huang, T., and Ma, J.: The 21st-century wetting inhibits growing surface ozone in Northwestern China, Atmospheric Chemistry and Physics, 25, 9669–9684, https://doi.org/10.5194/acp-25-9669-2025, 2025b.

Zhang, Y., Zhang, Y., Liu, Z., Bi, S., and Zheng, Y.: Analysis of Vertical Distribution

Changes and Influencing Factors of Tropospheric Ozone in China from 2005 to 2020 Based on Multi-Source Data, International Journal of Environmental Research and Public Health, 19, 12653, https://doi.org/10.3390/ijerph191912653, 2022.

Zhou, M., Li, Y., and Zhang, F.: Spatiotemporal Variation in Ground Level Ozone and Its Driving Factors: A Comparative Study of Coastal and Inland Cities in Eastern China, International Journal of Environmental Research and Public Health, 19, 9687, https://doi.org/10.3390/ijerph19159687, 2022.

Zhu, L., Wang, J., Xu, Y., Ma, N., Song, X., Qin, J., Li, B., Tsui, W. B. C., Lv, L., and Zhang, T.: Vertical Characteristics of an Ozone Pollution Episode in Hong Kong Under the Typhoon Mawar—A Case Study, Remote Sensing, 17, 3904, https://doi.org/10.3390/rs17233904, 2025a.

Zhu, X., Wang, H., Han, Y., Zhang, D., Liu, S., Zhang, Z., and Liu, Y.: Reconstructing the VOC–Ozone Research Framework Through a Systematic Review of Observation and Modeling, Sustainability, 17, 7512, https://doi.org/10.3390/su17167512, 2025b.

Zou, T., Xing, C., Xue, J., Li, Q., Tan, W., Wu, Z., and Liu, C.: Transport characteristics of urban and rural aerosols based on vertical observations and deep learning predictions, Atmospheric Research, 315, 107876, https://doi.org/10.1016/j.atmosres.2024.107876, 2025.